This is a pre-copyedited, author-produced version of an article accepted for publication in Journal of Petrology following peer review. The version of record Brown, C. R., Yakymchuk, C., Brown, M., Fanning, C. M., Korhonen, F. J., Piccoli, P. M., & Siddoway, C. S. (2016). From Source to Sink: Petrogenesis of Cretaceous Anatectic Granites from the Fosdick Migmatite–Granite Complex, West Antarctica. Journal of Petrology, 57(7), 1241–1278 is available online at: https://doi.org/10.1093/petrology/egw039

From source to sink: Petrogenesis of Cretaceous anatectic granites from the Fosdick migmatite–granite complex, West Antarctica

C.R. BROWN[1], C. YAKYMCHUK[1,2*], M. BROWN[1], C.M. FANNING[3], F.J. KORHONEN[4], P.M. PICCOLI[1] AND C.S. SIDDOWAY[5]

[1]LABORATORY FOR CRUSTAL PETROLOGY, DEPARTMENT OF GEOLOGY, UNIVERSITY OF MARYLAND, COLLEGE PARK, MARYLAND 20742, USA

[2]DEPARTMENT OF EARTH AND ENVIRONMENTAL SCIENCES, UNIVERSITY OF WATERLOO, WATERLOO, ONTARIO, N2L 3G1, CANADA

[3]RESEARCH SCHOOL OF EARTH SCIENCES, THE AUSTRALIAN NATIONAL UNIVERSITY, MILLS ROAD, CANBERRA ACT 0200, AUSTRALIA

[4]GEOLOGICAL SURVEY OF WESTERN AUSTRALIA, EAST PERTH WA 6004, AUSTRALIA

[5]DEPARTMENT OF GEOLOGY, THE COLORADO COLLEGE, COLORADO SPRINGS, COLORADO 80903, USA

*Corresponding author: Telephone: +1 519 888 4567 (x33763). Email: cyakymchuk@uwaterloo.ca

Running Title: Anatectic granite, West Antarctica

ABSTRACT

Anatectic granites from the Fosdick migmatite–granite complex yield U–Pb zircon crystallization ages that range from 115 Ma to 100 Ma, with a dominant grouping at 107–100 Ma, which corresponds to the timing of dome formation during the regional oblique extension that facilitated exhumation of the complex. The occurrence of leucosome-bearing normal-sense shear zones in migmatitic gneisses indicates that suprasolidus conditions in the crust continued into the early stages of doming and exhumation of the complex. The structure allows access to variably oriented granites in networks of dykes at deeper structural levels and sub-horizontal sheeted granites at shallower structural levels within the complex. This feature enables an evaluation of the mechanisms that modify the composition of granite melts in their source and of granite magmas during their ascent and emplacement using whole-rock major, trace element and Sr and Nd isotope compositions, zircon Hf and O isotope compositions, and phase equilibria modelling of potential source rocks. Geochemical variability within the granites is attributed to source heterogeneity and blending of melts, which themselves are consistent with derivation from regional metasedimentary and metaplutonic source materials. The granites typically contain coarse blocky K-feldspar and, or, plagioclase grains within interstitial quartz, and have low Rb/Sr ratios and large positive Eu anomalies. These features are inconsistent with the composition of primary crustal melts derived from metasedimentary and metaplutonic source materials, but consistent with early fractional crystallization of feldspar and subsequent drainage of the fractionated melt. Processes such as peritectic mineral entrainment and accessory mineral dissolution, entrainment and crystallization did not have any significant influence on the major and trace element composition of the granites. The granites in the networks of dykes are interpreted to represent choking of magma transport channels through the middle crust as the rate

of magma flow declined during doming and exhumation, whereas the sheeted granites record collapse of sub-horizontal, partially crystallized layers of magma by filter pressing and melt exfiltration during vertical shortening associated with doming and exhumation. These processes separated feldspar-rich residues from evolved melt. Based on the results of this study, caution is urged in estimating melt proportion from the volume of granite retained in migmatitic gneiss domes, since the granites may not represent liquid compositions.

KEY WORDS: *cumulate granite, Hf and O isotope geochemistry, migmatite, Nd–Sr isotope geochemistry, zircon*

INTRODUCTION

The generation and segregation of granite melt in the deep crust followed by extraction, ascent and emplacement of magma into the shallow crust are important processes by which the continental crust has become differentiated into a depleted lower portion and a complementary enriched upper portion (Sawyer *et al.*, 2011; Brown, 2013). Reworking of the crust by these processes plays a major role in the redistribution of mass and energy within the continents as well as the heat-producing elements. This has important implications for the tectonic history of large hot mountain belts (Jamieson *et al.*, 2011), cooling ultrahigh-temperature (UHT) metamorphic terranes (Korhonen *et al*., 2013), priming the crust for future UHT metamorphic events (Brown & Korhonen, 2009; Clark *et al.*, 2011), the particular style of some Proterozoic 'hot' orogens (McLaren & Powell, 2014), and the long-term stability of the continental crust (Sandiford & McLaren, 2002).

The composition of melt produced by fluid-absent hydrate-breakdown reactions in deep crustal settings has been determined from experimental melting studies (Skjerlie *et al*., 1993; Patiño Douce & Harris, 1998; Koester *et al.*, 2002), the analysis of former melt inclusions in peritectic minerals (Cesare *et al.*, 2007; Acosta-Vigil *et al.*, 2007; Ferrero *et al.*, 2011, 2012, 2014; Bartoli *et al.*, 2013) and thermodynamic modelling (White *et al.*, 2011). However, the liquid compositions obtained in these studies may not be representative of the melt extracted from the deep crust during anatexis due to processes operating throughout extraction and ascent, including: peritectic mineral entrainment and dissolution (Brown *et al.*, 1999; Villaros *et al.*, 2009; Taylor & Stevens, 2010; Clemens & Stevens, 2012); mixing between magmas of different sources (e.g. Kemp *et al.*, 2007); variable rates of accessory mineral dissolution and melt

extraction (Sawyer, 1991; Watt & Harley, 1993; Zeng *et al.*, 2005*a*, *b*, *c*); fractional crystallization during melt segregation, transport and emplacement (e.g. Sawyer, 1987; Milord *et al.*, 2001; Solar & Brown, 2001; Morfin *et al*., 2014); and source heterogeneity (e.g. Hill *et al*., 1986; Deniel *et al*., 1987; Pressley & Brown, 1999). Using benchmarks from experiments, melt inclusions and thermodynamic modelling of source materials, residua and granites enables these processes to be discriminated.

In Marie Byrd Land, West Antarctica, the Fosdick migmatite–granite complex (hereafter the Fosdick complex) is exposed in a mid-Cretaceous syn-anatectic structural dome. Given the oblique section through the crust provided by the dome, the Fosdick complex offers a rare opportunity to evaluate the processes that may modify the composition of anatectic magmas in the source, while migrating through the mid-crust and during emplacement contemporaneous with dome formation.

The timing of polyphase metamorphism, deformation and granite crystallization in the Fosdick complex is well characterized (Korhonen *et al.*, *2010a, b*; Yakymchuk *et al.*, 2015a). In this study we are concerned with the petrogenesis of granites related to the mid-Cretaceous tectonic event. After a summary of the geology of the Fosdick complex, we describe the field relationships and petrology of the gneisses and granites. We use U–Pb zircon geochronology to distinguish Cretaceous granites from older rocks and to assess the duration of granite crystallization in relation to doming. Elemental and isotope geochemistry of lower grade rocks from outside the Fosdick complex and for gneisses and granites from the inside the complex are used to assess source heterogeneity and to determine the contribution of different source components to the granites. The lower grade rocks exposed outside the Fosdick complex are isotopically similar to the gneisses inside the complex. Therefore, these protolith compositions

may be used to model maximum melt production during the Cretaceous event. The geochemical data are also used to assess processes such as fractional crystallization, peritectic mineral entrainment and accessory mineral dissolution, entrainment and crystallization on the compositional evolution of granite magma during syn-tectonic transport and emplacement.

REGIONAL GEOLOGY

West Antarctica

In the Phanerozoic, the continental margin of East Gondwana was an active convergent plate margin that stretched from eastern Australia through Antarctica to South America (Veevers, 2012; Fig. 1). A diachronous shift from oblique convergence to oblique divergence along the plate margin during the Albian predated the development of the West Antarctic rift system that eventually separated Zealandia, a continental terrane that includes the Western Province of New Zealand, from West Antarctica (Weaver *et al*., 1994; Mukasa & Dalziel, 2000; Tulloch *et al*., 2009*b*; McFadden *et al.*, 2010*a*,*b*).

Marie Byrd Land

Outside the Fosdick Mountains

Marie Byrd Land lies along the eastern side of the Ross Sea in West Antarctica (Fig. 1). The oldest exposed unit in western Marie Byrd Land is the Cambrian–Ordovician Swanson Formation, a sub-greenschist to greenschist facies folded and cleaved metaturbidite sequence with detrital zircon ages indicating derivation from granite in the Ross–Delamerian orogen and largely unexposed Proterozoic basement (Adams, 1986; Pankhurst *et al*., 1998; Yakymchuk *et al.*, 2015b). The Devonian–Carboniferous calc-alkaline Ford Granodiorite suite was intruded into

the Swanson Formation. These granodiorites have yielded whole rock Rb–Sr isochron and SHRIMP U–Pb zircon ages in the range 375–339 Ma (Adams, 1987; Pankhurst *et al*., 1998; Siddoway & Fanning, 2009; Tulloch *et al*., 2009*a*; Yakymchuk *et al.*, 2015b).

The Fosdick migmatite–granite complex

In the Fosdick Mountains, Cretaceous extensional deformation has exposed an 80 km by 15 km elongate dome of deeper crustal rocks comprising migmatitic gneisses and granites. The Fosdick complex is bounded to the north by an inferred steep dextral strike-slip fault (Siddoway *et al*., 2004, 2005), and to the south by the South Fosdick detachment, a south-dipping, dextral oblique detachment zone (McFadden *et al*., 2010*a*). The complex comprises layered sequences of migmatitic paragneisses and orthogneisses, and associated granites that are cross-cut by mafic dykes (Fig. 2; Richard *et al.*, 1994). Based on whole-rock geochemistry and a similar distribution of detrital zircon age populations from the paragneisses, the migmatitic gneisses are inferred to be the high-grade metamorphic equivalents of the Swanson Formation and the Ford Granodiorite suite (Siddoway *et al.*, 2004; Korhonen *et al*., 2010*b*; Yakymchuk *et al.,* 2013*a*, 2015b).

The Fosdick complex comprises several lithological units that consist of similar rock types but in different proportions (Korhonen *et al.*, 2010*a*; McFadden *et al*., 2010*a*; Yakymchuk *et al.*, 2013*b*). In the western and central Fosdick Mountains, at deeper structural levels in the complex, a layered plutonic sequence of migmatitic orthogneisses with minor granites and migmatitic paragneisses dominates much of the outcrop from Mt Iphigene to Mt Lockhart (Fig. 2). In the extreme west of the study area and around Mt Avers in the centre (Fig. 2), a thick unit of residual migmatitic paragneiss comprising biotite–sillimanite bearing melanosomes and garnet and, or, cordierite bearing leucosomes dominates the outcrops, and orthogneisses are rare . The

leucosomes commonly link to granite in dykes that cut across the layering. In the eastern Fosdick Mountains, at shallower structural levels, a sheeted leucogranite complex dominates the outcrop from Mt Bitgood to Bird Bluff (Fig. 2). This unit is composed of thick subhorizontal leucogranites interlayered with thinner migmatitic paragneiss and orthogneiss horizons. A prominent subhorizontal foliation is defined by biotite and sillimanite and is parallel to alternating leucogranite sheets and layers of gneiss. Cretaceous mafic dykes in this unit are generally folded and boudinaged (Siddoway *et al*., 2005; McFadden *et al*., 2010*a*; Saito *et al.*, 2013).

Based on U–Pb zircon and monazite ages, two episodes of regional metamorphism and crustal anatexis affected the Fosdick complex, one related to arc magmatism in the Devonian–Carboniferous and a second higher-grade event due to crustal thickening in the Lower Cretaceous (Siddoway *et al.*, 2004; Korhonen *et al.*, 2010*a*, *b*, 2012). Anatectic granites were produced during both metamorphic events (Siddoway *et al*., 2004; Korhonen *et al*., 2010*b*; Yakymchuk *et al*., 2015a). Devonian–Carboniferous metamorphism is cryptic due to the Cretaceous overprint, but it is unambiguously recorded by Carboniferous-age cores in monazite grains with Cretaceous rims (Korhonen *et al*., 2012; Yakymchuk *et al*., 2015a). The pressure (*P*) and temperature (*T*) conditions of this metamorphism have proven difficult to constrain due to uncertainty about the age of peritectic garnet (Korhonen *et al*., 2012). However, recent Lu–Hf garnet geochronology indicates that garnet is part of the Cretaceous metamorphic phase assemblage (Yakymchuk *et al.*, 2015a). Without garnet in the phase assemblage, peak conditions of the older metamorphic event are estimated to have been 680–800°C at 0·60–0·95 GPa (Yakymchuk *et al.*, 2015a).

For the Cretaceous metamorphism, Korhonen *et al*. (2010*a*) and Yakymchuk *et al.* (2015a) calculated peak metamorphic conditions of 830–870°C at 0·60–0·75 GPa. The significantly higher temperatures for the younger metamorphism, combined with the monazite and garnet geochronology, indicate that the dominant anatectic event in the formation of the migmatitic gneisses occurred during the Cretaceous. Mafic dykes were emplaced into the Fosdick complex during and after final crystallization of residual melt within the migmatitic gneisses.

FIELD RELATIONS AND PETROGRAPHY

Swanson Formation

Outside the Fosdick Mountains, the Swanson Formation is dominated by poorly sorted metagreywackes with subordinate amounts of slate and phyllite and rare ovoid calcareous nodules. Finer-grained layers have proportionally more biotite and less quartz; the schistosity is defined by the parallel alignment of biotite.

Ford Granodiorite suite

The Ford Granodiorite suite is well exposed outside the Fosdick Mountains, where it forms kilometer-scale plutons that crop out as isolated peaks. The Ford Granodiorite suite ranges in composition from granodiorite to monzogranite, with the former being the most common (Weaver *et al.*, 1991; Yakymchuk *et al.*, 2015*b*). These rocks are generally equigranular, although some outcrops are porphyritic with plagioclase phenocrysts, and typically unfoliated. Brown biotite dominates over green hornblende as the dominant ferromagnesian mineral.

The Fosdick complex

Migmatitic gneisses

Paragneiss Migmatitic paragneiss is composed of alternating thicker metapelite layers, up to several tens of centimeters thick, and thinner metapsammite layers (Fig. 3a). Leucosome is concentrated in the metapelite layers, defining a stromatic layering that is generally parallel to primary compositional layering and sub-horizontal to shallow-dipping throughout the Fosdick complex. Leucosomes up to 30 cm thick make up 43–72 vol. % of the outcrop (Yakymchuk *et al.,* 2013*b*); they comprise quartz, plagioclase and K-feldspar, with or without biotite, garnet and cordierite (Fig. 3b). Melanosomes are finer grained than leucosomes and typically contain biotite, quartz, cordierite, garnet, sillimanite, plagioclase, K-feldspar, and rare oxides. Accessory monazite, zircon and apatite are found as inclusions in the rock-forming minerals or along grain boundaries.

Orthogneiss Migmatitic orthogneiss is more homogeneous than the paragneiss (Fig. 3c). There is a shallow to moderately dipping foliation defined by the parallel alignment of individual biotite grains. Stromatic leucosomes, which are continuous over >20 cm and range from a few cm up to 2 m thick, form an anastomosing network rather than the strongly defined layering of the migmatitic paragneiss (Fig. 3c). Associated melanosomes comprise quartz, plagioclase, K-feldspar and biotite, with or without garnet. The stromatic leucosomes, which are in petrographic continuity with leucosome in normal-sense shear zones (Fig. 3c), have the same mineralogy as the melanosome, but commonly with coarse tabular feldspar phenocrysts and lesser amounts of biotite and garnet (Fig. 3d). Cordierite is rare and typically occurs in discordant leucosomes as

inclusion free euhedral grains. Accessory zircon, monazite and apatite occur as inclusions in the rock-forming minerals or along grain boundaries.

Cretaceous granites Cretaceous granites throughout the Fosdick complex exhibit a range of field relationships with the host-rock, have variable mineralogy and microstructures, and may be heterogeneous at the dm- to m-scale. Individual granite bodies vary from dykes to tabular sills (Fig. 4a–d) and range from dm to dacametres thick. In the east, at shallower structural levels, most granites are concordant with the dominant sub-horizontal foliation throughout the Fosdick complex (Fig. 4a), whereas to the west at deeper structural levels, the granites tend to be discordant (Fig. 4b–e), in some cases intersecting to form cylindrical structures (Fig. 4b) that may represent conduits for faster melt transport (Brown, 2013). These discordant granites generally show petrographic continuity with concordant leucosome and granite in the host-rock, and have similar mineralogy, mode and grain size (Fig. 4f), which is inferred to record simultaneous final crystallization. Thus, the leucosomes and granites are interpreted to have formed part of the same melt extraction network (e.g. Yakymchuk *et al.*, 2013*b*). Schollen of paragneiss, orthogneiss and mafic rock are commonly present aligned parallel to the layering in the wall-rocks (Fig. 4a), and schlieren of biotite ± garnet ± cordierite occur locally in the smaller granite dykes and towards the margins of larger dykes.

Granites are generally coarse-grained (2–10 mm), but some individual bodies contain discontinuous layers with different mean grain sizes. Discordant granites are commonly coarser-grained in the centre and finer-grained towards the margins; they are biotite-bearing, leucocratic and locally may contain up to 30 vol.% garnet or cordierite. Many granites contain blocky euhedral plagioclase or K-feldspar with interstitial quartz (Fig. 5).

Nine Cretaceous granites from the Fosdick complex were the focus of this study. Samples 10CY-039, Y1-AE064 and Y1-AW038 are biotite ± garnet granites collected from Mt Avers in the Central Fosdick Mountains; they are characterized by coarse-grained K-feldspars. The remaining six samples are from Mt Avers (Y1-AE033, Y1-AE051; C6-AW86-1) and Mt Iphigene (Y1-IG052, Y1-IG062, and Y1-IG070); they are coarse-grained biotite ± garnet ± cordierite granites with euhedral tabular plagioclase and K-feldspar. In addition, ten Cretaceous granites for which analytical data were previously reported in Korhonen *et al.* (2010*b*) are included in the discussion of granite petrogenesis.

ANALYTICAL METHODS

U–Pb zircon geochronology

Zircon U–Pb geochronology was used to determine the age of the orthogneiss protoliths and to evaluate the timing of Cretaceous granite crystallization in the Fosdick complex. Two different analytical techniques were used during this study, as discussed below.

Sensitive high-resolution ion microprobe (SHRIMP)

U–Pb zircon age determinations were made using SHRIMP II and SHRIMP-RG at the Australian National University Research School of Earth Sciences (ANU-RSES) following the procedures described in Williams (1998 and references therein) and using a spot size of ~20 μm. Data were reduced using the SQUID Excel Macro (Ludwig, 2001). The zircon U/Pb ratios have been normalized relative to a value of 0·0668 for the Temora reference zircon, equivalent to an age of 417 Ma (Black *et al*., 2003); analytical uncertainties for the respective analytical sessions

are given in the footnotes to Supplementary Data Electronic Appendix Table 1. Uncertainties reported for individual analyses (ratios and ages) are given at the 1σ level.

Laser-ablation inductively coupled plasma mass spectrometry (LA–ICP–MS)

Zircon grains (generally 50–100) were incorporated into a 1" epoxy mount together with fragments of the Sri Lanka standard zircon at the University of Arizona. The mounts were sanded down to a depth of ~20 microns, polished, imaged, and cleaned prior to isotopic analysis. U–Pb geochronology of zircons was conducted by laser ablation multicollector inductively coupled plasma mass spectrometry (LA-MC-ICP-MS) at the Arizona LaserChron Center. The analyses involved ablation of zircon with a Photon Machines Analyte G2 excimer laser using a spot diameter of 30 μm, a fluence of ~5 J/cm^2 and a repetition rate of 7 Hz. Isotopes of U, Th and Pb were measured simultaneously using a Nu Plasma HR-ICP-MS. The complete analytical protocol is described in Gehrels *et al.* (2008). Results are provided in Supplementary Data Electronic Appendix Table 2.

For both SHRIMP and ICP–MS U–Pb zircon geochronology, Tera–Wasserburg (Tera & Wasserburg, 1972) concordia plots and weighted mean $^{238}U/^{206}Pb$ ages were calculated using ISOPLOT/EX (Ludwig, 2003). Where appropriate the "Mixture Modelling" algorithm of Sambridge & Compston (1994) via ISOPLOT/EX has been used to un-mix statistical age populations or groupings. From such groupings weighted mean $^{238}U/^{206}Pb$ ages have been calculated and the uncertainties reported as 95% confidence limits, including incorporation, in quadrature, of the uncertainty in the reference zircon calibration. These ages are summarized in Table 1.

Major oxide, trace element and REE chemistry

Whole-rock major and trace element compositions were determined for gneisses and granites to quantify the chemical variation of these rocks and, together with literature data, to evaluate the different processes that potentially could have modified anatectic melt compositions.

Major oxide and select trace elements were analysed by X-ray fluorescence spectrometry at Franklin and Marshall College. A PANanalytical 2404 X-ray fluorescence spectrometer equipped with a PW2540 X-Y sample handler was used following the procedures described by Boyd & Mertzman (1987). Fe_2O_3 was measured by XRF and FeO was determined by Fe^{2+} titration.

Rare earth elements were analysed by inductively coupled plasma mass spectrometry at the University of Maryland. Twenty milligrams of powdered sample was dissolved in closed Savillex® Teflon beakers using 0·5 ml of 14M HNO_3 and 3 ml of 29M HF. Samples were digested for 24 hours, dried down and subjected to a second dissolution in 0·25 ml 12M $HClO_4$, 0·5 ml of 14M HNO_3 and 3 ml of 29M HF for 72 hours. The solution was dried down, brought up in 6M HCl and dissolved for a further 24 hours; this last procedure was repeated until the sample was fully dissolved. Samples were diluted by a factor of 100. One ml of a 20 ppb ^{115}In solution was added to the diluted sample to enable correction for instrumental drift.

The following isotopes ^{115}In, ^{139}La, ^{140}Ce, ^{141}Pr, ^{143}Nd, ^{147}Sm, ^{153}Eu, ^{158}Gd, ^{159}Tb, ^{163}Dy, ^{165}Ho, ^{167}Er, ^{169}Tm, ^{173}Yb and ^{175}Lu were analysed using a Finnigan Element 2 single collector ICP-MS; solutions were introduced into the plasma using an APEX desolvating nebulizer. Concentrations were determined using a standard-bracketing method using USGS standards G-2, a granite, and MAG-1, a marine sediment. Element concentrations in gneisses and granites were determined using G-2 as the primary standard, whereas the concentrations of metasedimentary

and paragneiss samples were determined using MAG-1. Signals were corrected for instrumental drift, by normalizing all data to the ^{115}In signal in the G-2 standard, and the blank, which was <0·1% of the signal for standards and <0·7% of the signal for unknowns. Uncertainties from counting statistics ranged from 1% to 6%, and propagated uncertainties for concentrations ranged from 4% to 12%.

Whole-rock Rb, Sr, Sm and Nd isotope compositions

Whole-rock isotope compositions were acquired to evaluate the heterogeneity of the inferred source rocks and the granites, and to quantify the relative contributions of possible source components to granite petrogenesis.

Rb, Sr, Sm and Nd isotope compositions were determined in the Isotope Geochemistry Laboratory at the University of Maryland. The rocks were prepared in a manner similar to that of Korhonen *et al.* (2010*b*). Fifty milligrams of powder were dissolved in Savillex® Teflon beakers using 3 ml of 29M HF and 0·5 ml of 14M HNO_3, together with isotopic spikes enriched in ^{87}Rb, ^{84}Sr, ^{149}Sm, and ^{150}Nd, using a closed digestion at 180–190ºC for 24 hours. Samples were dried and re-dissolved in 3 ml of 29M HF, 0·5 ml of 14M HNO_3, and 0·25 ml of 12M $HClO_4$, and digested for a further 72 hours at 180–190ºC, then dried. To finish, 2 ml of 6M HCl was added to the samples, which were digested at 180ºC for 24 hours and dried again; this last procedure was repeated until the resulting solution was clear, after which samples were finally dried and brought up in 2 ml of 2·5M HCl.

Rubidium, Sr and REE were separated from each other using a primary cation exchange column filled with AG50Wx4 (200–400 mesh) resin. Samples were loaded in chloride form. Rubidium and Sr were eluted in 2·5M HCl, while the REE were eluted from the column in 6M

HCl. Rubidium cuts were dried and diluted in 2% HNO_3. Strontium cuts were passed through a cleanup column filled with Eichrom™ Sr-spec resin and eluted in 0·05M HNO_3. The REE cuts from the primary column were passed through a secondary column filled with 0·225M 2-methyllactic acid (MLA). Samarium and Nd were eluted in 0·225M MLA (pH = 4·67).

Strontium, Nd and Sm isotope ratios were analysed using a VG Sector 54 TIMS or a Nu Plasma multi-collector (MC) ICP-MS. Samples 10CY-003, Y1-AW039, Y1-CB080, Y1-IG070, and Y1-LH077 were analyzed for Nd using a Nu Plasma multi-collector (MC) ICP-MS. Sample 10CY-039 was analysed for Sm also using the Nu Plasma ICP-MS. For the remaining samples, Sr, Nd and Sm isotope ratios were analysed using TIMS. Rubidium ratios were measured using a Nu Plasma MC-ICP-MS at the University of Maryland. Samples were diluted by a factor of 100 and were introduced into the plasma using an Aridus I desolvating nebulizer. A 50 ppb Rb SpecPure® plasma standard was introduced after every three sample analyses and was used to correct for instrumental fractionation and drift. Rubidium blanks averaged 8·04 ppm (n = 4), <1% of the sample Rb concentrations.

Strontium cuts (~390 ng) were loaded onto a single Re filament with a Ta-oxide activator, and analysed in a multi-dynamic mode. Strontium isotopes were corrected for mass fractionation by normalizing the measured $^{87}Sr/^{86}Sr$ ratio to an $^{86}Sr/^{88}Sr$ ratio = 0·1194. The mass fractionation and spike corrected $^{87}Sr/^{86}Sr$ ratio was normalized to an average SRM 987 $^{87}Sr/^{86}Sr$ value of 0.71034 (NIST) to correct for instrumental bias. Strontium blank concentrations averaged 14·0 ng (n = 4), <1% of sample Sr concentrations.

Neodymium cuts (~200 ng) were loaded on two Re filaments with phosphoric acid and loaded into the machine in a triple filament arrangement. Neodymium ratios were measured in dynamic mode and corrected for mass fractionation by normalizing the measured $^{143}Nd/^{144}Nd$

ratio to $^{146}Nd/^{144}Nd = 0{\cdot}7219$. All $^{143}Nd/^{144}Nd$ ratios measured in the samples were corrected for instrumental bias to an AMES standard $^{143}Nd/^{144}Nd$ value of 0·512153 (in-house TIMS measurements). Samarium was measured in static mode. Samarium blanks averaged 0·311 ng (n = 3) while Nd blanks averaged 2·28 ng (n = 3); both <1% of sample Sm and Nd concentrations.

The USGS G-2 granite was analysed 7 times over a period of 12 months. Repeat analyses yielded an average $^{87}Sr/^{86}Sr$ of 0·709767 ± 0·000038 (n = 7) and an average $^{143}Nd/^{144}Nd$ of 0·512243 ± 0·000010 (n = 7). Rubidium concentrations averaged 167·6 ppm (range 162·9–174·2 ppm), Sr concentrations 488·8 ppm (range 482·1–496·2 ppm), which are slightly offset from the USGS recommended values of 170 ± 3 ppm for Rb and 478 ± 2 ppm for Sr. Samarium concentrations averaged 7·1 ppm (range 7·0–7·3 ppm), Nd concentrations 52·6 ppm (range 52·2–53·2 ppm), which are within uncertainty of the USGS recommended values of 7.2 ± 0.7 for Sm and 55 ± 6 for Nd.

Lu–Hf and O analysis of zircon

Hf and O isotope compositions of zircon were determined to quantify heterogeneity of the inferred source rocks and the granites, and to assess the relative contribution of possible source components to the petrogenesis of the granites.

Following the U–Pb analyses, the SHRIMP 1–2 μm deep U–Pb pits were lightly polished away and oxygen isotope analyses made in the same location using a SHRIMP II fitted with a Cs ion source and electron gun for charge compensation as described by Ickert *et al.* (2008). Oxygen isotope ratios were determined in multiple collector mode using an axial continuous electron multiplier (CEM) triplet collector, and two floating heads with interchangeable CEM–Faraday Cups. The Temora 2 and FC1 reference zircons were analysed to monitor and correct for

isotope fractionation. The measured $^{18}O/^{16}O$ ratios and calculated $\delta^{18}O$ values have been normalised relative to an FC1 weighted mean $\delta^{18}O$ value of +5·4 ‰ (Ickert *et al*, 2008). Reproducibility in the Duluth Gabbro FC1 reference zircon $\delta^{18}O$ value ranged from ± 0·30‰ to 0·37‰ (2σ uncertainty) for the analytical sessions. As a secondary reference, the Temora 2 zircon was analysed in the same sessions, which gave $\delta^{18}O$ values of +8·2‰ in agreement with data reported by Ickert *et al.* (2008).

Lu–Hf isotope measurements were conducted by laser ablation multicollector inductively coupled plasma mass spectroscopy (LA–MC–ICP-MS) using the ANU-RSES Neptune MC–ICP-MS coupled with a 193 nm ArF Excimer laser, following procedures similar to those described in Munizaga *et al.* (2008). For all analyses of unknowns or secondary standards, the laser spot size was ~47 μm in diameter. Laser ablation analyses targeted the same locations within single zircon grains used for both the U–Pb and oxygen isotope analyses described above. The mass spectrometer was first tuned to optimal sensitivity using a large grain of zircon from the Mud Tank carbonatite. Isotopic masses were measured simultaneously in static collection mode. A gas blank was acquired at regular intervals throughout the analytical session (every 12 analyses). Typically the laser was fired with a 5–8 Hz repetition rate and 50–60 mJ energy. Data were acquired for 100 seconds, but in many cases only a selected interval from the total acquisition was used in data reduction.

Throughout the analytical session several widely used reference zircons were analysed to monitor data quality and reproducibility. Signal intensity was typically ~5–6 V for total Hf at the beginning of ablation, and decreased over the acquisition time to 2 V or less. Isobaric interferences of ^{176}Lu and ^{176}Yb on the ^{176}Hf signal were corrected by monitoring signal intensities of ^{175}Lu and ^{173}Yb, ^{172}Yb and ^{171}Yb. The calculation of signal intensity for ^{176}Hf also

involved independent mass bias corrections for Lu and Yb (see Munizaga *et al.* (2008) for further details). During the course of data collection the reference zircons gave the following weighted mean $^{176}Hf/^{177}Hf$ ratios: 91500 = 0·282310 ± 14 (±2σ) for 23 analyses, Mud Tank = 0·282516 ± 11 for 8 analyses, FC1 = 0·282173 ± 9 for 22 of 23 analyses, Plesovice = 0·282486 ± 11 for 16 of 17 analyses, and Monastery = 0·282744 ± 12 for 8 analyses. These are within analytical uncertainty of the values reported by Woodhead & Hergt (2005).

ZIRCON U–Pb GEOCHRONOLOGY

The Fosdick complex

Orthogneisses

Zircons from sample Y1-AW039 show oscillatory zoning in cathodoluminescence (CL) images; they are a mix of elongate and stubby, euhedral to anhedral grains and some have xenocrystic cores (Fig. 6). The LA-ICP-MS data from this sample yield a generally uniform age of 368·5 ± 5·3 Ma (Fig. 7; n = 15; MSWD = 1·1), which is interpreted as the crystallization age of the Ford Granodiorite suite protolith.

Zircons from sample Y1-IG053 are stubby to elongate, prismatic and oscillatory zoned in CL images; a few grains have bright, resorbed cores (Fig. 6). The LA-ICP-MS data for this sample yield a Devonian age of 366·8 ± 6·2 Ma (Fig. 7; n = 23 of 24; MSWD = 2·9). In contrast, SHRIMP data yield a range of dates from 390 to 345 Ma (with three dates of 533, 300 and 287 Ma), with a dominant group of 14 dates that yield an age of 366·6 ± 2·2 Ma (MSWD = 0·56), essentially the same as the LA-ICP-MS age (Figs 7, 8). The two younger SHRIMP dates of 300 and 287 Ma are from narrow dark rims that mantle bright oscillatory zoned cores. These younger dates are interpreted to result from modification by a process such as Pb loss during the

Cretaceous metamorphic overprint. Therefore, the *c*. 366 Ma age is interpreted to be the crystallization age of the Ford Granodiorite suite protolith.

Zircons from sample K6-B26 are elongate and prismatic with oscillatory zoning in CL images (Fig. 6). A minor population of zircon has resorbed bright oscillatory zoned cores mantled by dark rims (Fig. 6). SHRIMP data from zircons with simple oscillatory zoning in this sample yield a range of dates from *c*. 376 to *c*. 335 Ma, with three younger dates of 317, 285 and 105 Ma. A group of 17 of the oldest dates yield an age of 365·7 ± 2·1 Ma (Fig. 7; MSWD = 3·3). Two of the younger dates (317 and 285 Ma) are interpreted to result from Pb loss during the Cretaceous metamorphic overprint. A single date of *c.* 105 Ma, which is from a dark rim surrounding a resorbed and bright oscillatory-zoned core, is interpreted to represent new zircon growth from anatectic melt. This interpretation is supported by monazite U–Pb geochronology for this sample, which yielded exclusively Cretaceous ages (Korhonen *et al.*, 2012). The Devonian age is interpreted to be the crystallization age of the Ford Granodiorite suite protolith.

Oscillatory zoned zircons from sample Y1-AW049 are stubby to elongate and prismatic; a few grains have embayed cores (Fig. 6). LA-ICP-MS analysis of zircon cores and rims yields a Devonian age of 361·2 ± 6·2 Ma (Fig. 7; n = 19 of 20; MSWD = 1·8). Since high-grade metamorphism and anatexis of the orthogneiss is interpreted to be of Cretaceous age (Yakymchuk *et al.*, 2015a), the Devonian age retrieved from this sample is interpreted to be the crystallization age of the Ford Granodiorite suite protolith.

Zircons from Y1-MJ075 are stubby to elongate (Fig. 6). The LA-ICP-MS data yield dates that range from *c*. 1520 to *c*. 100 Ma for this sample, with a dominant population that gave an age of 115·5 ± 3·7 Ma (Fig. 7; n = 7; MSWD = 2·2), which is interpreted to date the Cretaceous high-grade metamorphic event.

Zircons from sample 10CY-035 are elongate and prismatic. They have bright cores with darker zoned mantles surrounded by very thin bright rims in CL images (Fig. 6). The LA-ICP-MS data for this sample yield a range of dates from *c*. 380 to *c*. 100 Ma, with three dominant populations at *c.* 360 Ma (n = 8) and *c.* 320 Ma (n = 6), from the darker zoned mantles, and *c.* 100 Ma (n = 4) from the bright rims (Fig. 7). The Cretaceous age group at *c*. 100 Ma is interpreted to record the Cretaceous metamorphic overprint, whereas the older age groups likely represent the Ford Granodiorite suite protolith age and the effects of Carboniferous recrystallization, respectively.

Cretaceous granites

Granites from Mt Iphigene (Y1-IG070, Y1-IG052) and from Mt Avers (Y1-AW038, Y1-AE033, 10CY-039, Y1-AE051, Y1-AE064) have zircons that are euhedral to anhedral with dark and generally unzoned cores mantled by bright oscillatory-zoned rims in CL images (Fig. 6, Table 1). LA-ICP-MS data from the bright rims yield weighted mean ages that range from *c*. 108 to *c*. 103 Ma (Fig. 7). High ^{204}Pb in the dark cores prohibits the calculation of meaningful ages.

Zircons from three of these granites were also analysed using the SHRIMP. For sample Y1-IG070, ^{206}Pb/^{238}U dates range from *c*. 115 to *c*. 104 Ma (with one date of *c*. 126 Ma); an older group defined an age of 113·2 ± 1·8 Ma (Fig. 8; n = 5; MSWD = 1·3), whereas a younger group yielded an age of 106·6 ± 1·1 Ma (Fig. 8; n = 10; MSWD = 1·7). The younger age is interpreted as the timing of crystallization, whereas the older age may represent grains scavenged during reworking of a slightly older Cretaceous component in the Fosdick complex, such as *c.* 115 Ma granites reported by Korhonen *et al.* (2010b) and McFadden *et al.* (2010a). For sample Y1-AW038, ^{206}Pb/^{238}U dates range from *c*. 117 to *c*. 102 (excluding two dates of *c*. 326 and *c*. 143

Ma); a group of younger dates yield an age of 103·0 ± 1·1 Ma (Fig. 8; n = 4; MSWD = 0·69), interpreted as the crystallization age of the granite. This age is younger than the LA-ICP-MS age (Fig. 7), which may have been affected by the larger laser spot size inadvertently sampling zircon from a slightly older Cretaceous component.

An additional granite from Mt Iphigene (Y1-IG062) yielded zircons that are zoned, and predominantly prismatic and euhedral, although a few grains have bright, zoned cores in CL images that show evidence of recrystallization (Fig. 7). This sample contains both Devonian–Carboniferous and Cretaceous zircon age populations, with three Permian dates (Figs 7, 8). The older population includes concordant dates from *c*. 393 to *c*. 324 Ma (LA-ICP-MS and SHRIMP); for the LA-ICP-MS data, 13 analyses define an age of 363·5 ± 3·9 Ma (Fig. 7; MSWD = 1·9), which likely reflects a population of zircon grains inherited from the Ford Granodiorite suite. The younger population includes concordant dates from *c*. 114 to *c*. 98 Ma (LA-ICP-MS and SHRIMP); no statistically significant age can be calculated from these data. Based on field relations as well as the Cretaceous zircon dates, this granite in interpreted to be of Cretaceous age.

GEOCHEMISTRY

Major oxide, trace element and rare earth element chemistry

Major oxide, trace element and rare earth element (REE) analyses are presented in Table 2. These data are combined with published data (Weaver *et al.*, 1991, 1992; Pankhurst *et al.*, 1998; Tulloch *et al.*, 2009*a*; Yakymchuk *et al.,* 2015*b*; Korhonen *et al.*, 2010*b*) and shown as variation

diagrams for major oxides and trace elements in Figs 9 and 10, and as chondrite-normalized REE patterns in Figs 11 and 12.

Swanson Formation

Samples of the Swanson Formation (n = 9) have SiO_2 contents ranging from 61 to 74 wt %; they are peraluminous with aluminum saturation indices (ASI= Molar [Al_2O_3/(CaO+Na_2O+K_2O)]) of 1·28–2·00 (Fig. 9). With increasing SiO_2, CaO, Na_2O and P_2O_5 remain relatively constant, whereas Al_2O_3, FeO*+MgO+TiO_2 and K_2O decrease (Fig. 9). With the exception of U, Zr and La, which are positively correlated with increasing SiO_2 (Fig. 10), and Rb and Rb/Sr, which are slightly negatively correlated with increasing SiO_2 (Fig. 10), trace element concentrations remain relatively constant (Fig. 10). The Swanson Formation exhibits a narrow range of REE abundances and smooth normalized REE patterns (Fig. 11) that are convex for the LREE (La–Sm), with La_N/Lu_N of 8·64–10·2 and have moderate negative Eu anomalies (Eu_N/Eu_N^* = 0·62–0·70).

Ford Granodiorite suite

Samples of the Ford Granodiorite suite (n = 24) have SiO_2 contents ranging from 64 to 76 wt % (Fig. 9); they are metaluminous to peraluminous, with ASI = 0·90–1·12 (Fig. 9). With increasing SiO_2, Al_2O_3, FeO*+MgO+TiO_2, CaO, P_2O_5, Ba, U, Sr and Zr generally decrease, Na_2O, La and Th remain relatively constant, and K_2O, Rb and Rb/Sr tend to increase (Figs 9, 10). These rocks have a wide range of REE abundances, smooth to convex LREE patterns and smooth to concave up HREE (Gd–Lu) patterns (Fig. 11), La_N/Lu_N of 2·3–9·92 and variable negative Eu anomalies (Eu_N/Eu_N^*=0·31–0·85).

The Fosdick complex

Paragneisses and orthogneisses Paragneisses have major oxide and trace element abundances, and geochemical trends that are similar to those for the Swanson Formation, although with more variability (Figs 9, 10). The aluminum saturation indices and Rb/Sr ratios tend to be higher than the Swanson Formation, whereas CaO, P_2O_5 and Sr tend to be lower. One biotite-rich paragneiss sample, Y1-IG057, has 42 wt % SiO_2, an ASI value of 3·13 and higher FeO*+MgO+TiO_2, Al_2O_3, Rb, Rb/Sr, and Th, and lower CaO, Na_2O, and Sr than the other samples. The paragneisses have a wider range of REE concentrations than the Swanson Formation, but otherwise show similar chondrite-normalized REE patterns (Fig. 11), with La_N/Lu_N of 6·3–22·2 and variable negative Eu anomalies (Eu_N/Eu_N^* = 0·17–0·90). Sample Y1-IG057 has elevated HREE compared with the other samples.

Orthogneisses have major oxide and trace element abundances and trends that are consistent with a Ford Granodiorite suite parentage (Figs 9, 10). However, the Al_2O_3 contents and ASI of the orthogneisses are slightly higher, whereas Th is lower (Figs 9, 10); K_2O is lower and P_2O_5 higher at low SiO_2 (Fig. 9). The orthogneisses have a wider range of REE concentrations than the Ford Granodiorite suite, with La_N/Lu_N of 7·7–116·8, more variability in the HREE patterns (Fig. 11), and, with one exception (10CY-035, Eu_N/Eu_N^* = 1·48), negative Eu anomalies (Eu_N/Eu_N^* = 0·33–0·96).

Cretaceous granites The granites have a limited range of silica contents (70–76 wt %), with ASI values similar to the orthogneisses. Al_2O_3, FeO*+MgO+TiO_2, Rb, Rb/Sr, Zr, La and Th are

generally negatively correlated with increasing SiO_2, whereas K_2O increases with increasing SiO_2 except for two high silica granites (Figs 9, 10). CaO, Na_2O, P_2O_5, Ba, U and Sr show no clear trend, although Ba and Sr are highly variable (Figs 9, 10). For major elements, there is no discernable difference between the garnet-present and the garnet-absent variants. However, the garnet-present granites generally have higher ΣHREE than the garnet-absent granites (Fig. 10). Although quite variable, decreasing Zr is correlated with decreasing ΣHREE, particularly in the garnet-absent granites, P_2O_5 is negatively correlated with increasing ΣLREE, and decreasing Th is weakly correlated with decreasing ΣLREE (Fig. 10).

The granites have lower ΣREE relative to their potential sources. Garnet-absent granites generally have low to moderate negatively sloping normalized REE patterns (La_N/Lu_N of 5.88–25·6), whereas the garnet-present granites have flatter concave-up normalized REE patterns with rising convex HREE, as expected from the presence of garnet (Fig. 12). Four of the garnet-absent granites have small negative Eu anomalies, one of which (C6-AW86-1) has a particularly steep normalized REE pattern (La_N/Lu_N = 82·6) showing strong depletion in the HREE with a concave up slope (Fig. 12). However, a majority of the garnet-absent and all but one of the garnet-present granites have variable, typically moderate to large positive Eu anomalies (Eu_N/Eu_N^* = 0·37–10·3); this variation is unrelated to SiO_2 content.

Sr and Nd isotope compositions

Nd and Sr isotope results for 20 samples are presented in Table 3 and are summarized, together with additional data from the literature, in Fig. 13. Although the Cretaceous metamorphism is the dominant anatectic event in the Fosdick complex, for completeness the Sr and Nd isotope

compositions for the migmatitic gneisses are reported at 360 and 100 Ma in Table 3, but are only plotted for 100 Ma in Fig. 13.

The Fosdick complex

Migmatitic gneisses Paragneiss samples have $^{87}Sr/^{86}Sr_{100Ma}$ values that vary from 0·71980 to 0·73344 and εNd_{100Ma} values that range from -10·5 to -8·7 (with one value of -13·1), generally consistent with values from the Swanson Formation (Fig. 13). Orthogneiss samples have $^{87}Sr/^{86}Sr_{100Ma}$ values that vary from 0·71238 to 0·72501 and εNd_{100Ma} values that range from -6·8 to -3·6 (with one value of -11·2), generally consistent with values from the Ford Granodiorite suite.

Cretaceous granites Granites within the Fosdick complex have $^{87}Sr/^{86}Sr_{100Ma}$ ratios that vary from 0·71169 to 0·73900 and εNd_{100Ma} values that range from -8·0 to -3·9 (Fig. 13).

Hf and O isotope compositions of zircon

Five samples were selected for Hf and O isotope analysis of zircon; the data are given in Table 4 and summarized, together with an additional sample (C6-AW86-1, data from Yakymchuk *et al.*, 2013*a*), in Figs 14 and 15.

Fosdick complex

Orthogneiss Sample Y1-IG053 contains zircon with εHf_{360} values of -4·3 to -0·2, $\delta^{18}O$ values of 8·3 to 9·3 (Fig. 14), and weighted means of -2·8 ± 0·4 and 8·8 ± 0·1, respectively (2σ; 19 of 20). Sample K6-B26 contains zircon with εHf values of -4·2 to -0·6, $\delta^{18}O$ values of 8·0 to 9·7 (Fig. 14), and weighted means of -2·1 ± 0·4 and 8·6 ± 0·2, respectively (2σ; 18 of 19). A single Cretaceous age spot yields εHf_{100} and $\delta^{18}O$ values of -6·1 and 9·8.

Cretaceous granites Sample Y1-AW038 contains zircon with εHf_{100} values of -6·6 to -3·3, $\delta^{18}O$ values of 8·8 to 9·9 (Fig. 15), and weighted means of -5·0 ± 0·3 and 9·3 ± 0·2, respectively (2σ; n = 18). Sample Y1-IG070 contains zircon with εHf_{100} values of -7·1 to -4·0, $\delta^{18}O$ values of 8·7 to 10·3 (Fig. 15), and weighted means of -5·3 ± 0·5 and 9·4 ± 0·3, respectively (2σ; n = 13).

Sample Y1-IG062 contains both Devonian–Carboniferous and Cretaceous zircon (Fig. 15a). Devonian–Carboniferous zircon spots have εHf_{360} values of -5·9 to -1·9, $\delta^{18}O$ values of 8·8 to 10·2, and weighted means of -3·1 ± 0·6 and 9·4 ± 0·2, respectively (2σ; 12 of 13). Cretaceous zircon spots have εHf_{100} values of -7·3 to -1·7, $\delta^{18}O$ values of 9·5 to 10·2, and weighted means of -4·2 ± 1·4 and 9·8 ± 0·2, respectively (2σ; n = 9). Devonian–Carboniferous zircon εHf values recalculated to 100 Ma are -11·6 to -7·5, which is less radiogenic than most Cretaceous zircon. Furthermore, Cretaceous zircons generally have higher $\delta^{18}O$ values than Devonian–Carboniferous zircons (Fig. 15a).

PHASE EQUILIBRIA MODELLING OF SOURCE ROCKS

The migmatitic gneisses in the Fosdick complex show unambiguous evidence of partial melting and melt loss during the Cretaceous (Korhonen *et al.*, 2012; Yakymchuk *et al.*, 2015a). However,

it is likely that partial melting and melt loss also occurred during the Devonian–Carboniferous subduction-related metamorphism, at least in the Swanson Formation protoliths. Indeed, this is suggested by the occurrence of Carboniferous S-type granites south of the Fosdick complex (Tulloch *et al.*, 2009*a*). If we assume the possibility of melt loss during the Devonian–Carboniferous metamorphism, it becomes unclear whether the paragneisses or the orthogneisses were more fertile during the Cretaceous event.

For the crustal level exposed in the Fosdick complex, previous forward modelling of phase equilibria for Swanson Formation and Ford Granodiorite suite compositions, the putative protoliths of the gneisses, suggested that the former could have produced up to 30 vol. % melt but the latter less than 5 vol. % melt at the peak of Cretaceous metamorphism (Korhonen *et al.*, 2010*a*). However, if some melt was generated and lost during the Devonian–Carboniferous subduction-related metamorphism, these estimates will be maxima. To assess the effect of the Devonian–Carboniferous metamorphism and melting on the fertility of the gneisses during the Cretaceous event we use phase equilibria forward modelling.

Methods

Calculations were performed using THERMOCALC v.3.35 (Powell & Holland, 1988) and the internally consistent dataset of Holland & Powell (1998). Modelling was undertaken in the Na_2O–CaO–K_2O–FeO–MgO–Al_2O_3–SiO_2–H_2O–TiO_2–Fe_2O_3 (NCKFMASHTO) chemical system. *P–T* pseudosections were calculated for representative samples of the Swanson Formation (sample 10CY-002) and the Ford Granodiorite suite (sample R7218 from Weaver *et al*., 1991) from outside the Fosdick complex, and for a representative migmatitic paragneiss (sample 10CY-015) and orthogneiss (sample Y1-IG053) from inside the Fosdick complex. The

FeO content of these samples was determined by Fe^{2+} titration and Fe_2O_3 contents were calculated by difference. For sample R7218 (Ford Granodiorite Suite), 10% of the total iron is assumed to be ferric (Table 5). For the protolith samples (samples 10CY-002 and R7218), the amount of water in the bulk compositions was adjusted so that there was minimal (~0.01 mol%) free H_2O at the solidus at 0.7 GPa, which is consistent with fluid-absent conditions above the solidus (White & Powell, 2002; White *et al.*, 2005). If the actual prograde path crossed the solidus at lower or higher pressures, this approach would slightly overestimate or underestimate the quantity of melt produced, respectively. For the migmatitic gneisses (samples 10CY-015 and Y1-IG053), the amount of H_2O in the bulk compositions was adjusted from the measured loss on ignition value so that the observed mineral assemblage was stable just above the solidus, which reflects the conditions at which this assemblage was in equilibrium with the last remnants of melt (cf. White *et al.*, 2004; Diener *et al.*, 2008; Korhonen *et al.*, 2010*a*).

The phases considered are: Bt – biotite; Crd – cordierite; Di – diopside; Ep – epidote; Grt – garnet; H_2O – aqueous fluid; Ilm – ilmenite; Kfs – K-feldspar; Ky – kyanite; Liq – silicate liquid/melt; Mag – magnetite; Ms – muscovite; Opx – orthopyroxene; Pl – plagioclase; Pg – paragonite; Qtz – quartz; Rt – rutile; Sil – sillimanite; Spl – spinel; Ttn – titanite. The activity–composition (*a*–*x*) models for the phases considered are: biotite, garnet, and melt (White *et al.*, 2007); orthopyroxene and spinel–magnetite (White & Powell, 2002); cordierite and epidote (Holland & Powell, 1998); K-feldspar and plagioclase (Holland & Powell, 2003); white mica (Coggon & Holland, 2002); ilmenite–hematite (White *et al.*, 2000); clinopyroxene (Green *et al.*, 2007); and hornblende (Diener *et al.*, 2007). Phases modelled as pure end-members are: quartz, rutile, titanite, aqueous fluid (H_2O), kyanite and sillimanite.

Results of phase equilibria modelling

P–T pseudosections for the representative samples are shown in Fig. 16. These phase diagrams show the stable phase assemblage and the amount of melt (as mol. % (~vol. %) isopleths) generated in a closed (undrained) system at *P–T* for each composition. Peak conditions for the Devonian–Carboniferous metamorphic event are estimated to have been 680–800°C at 0·60–0·95 GPa (Yakymchuk *et al*., 2015*a*). At these *P–T* conditions, the Swanson Formation composition could have produced up to 10 mol. % melt, but the Ford Granodiorite suite composition would have produced <1 mol. % melt (Fig. 16a, b). Melt drainage from the suprasolidus crust is expected when the proportion of melt reaches ~7 vol. % (e.g. Rosenberg & Handy, 2005; Brown, 2010). Therefore, the Swanson Formation composition modeled was likely to have lost melt at least once during the Devonian–Carboniferous event, resulting in a less fertile composition for melting during the Cretaceous. Although there is variation in the fertility of the Swanson Formation, this confirms that the melt volumes predicted by Korhonen *et al.* (2010*a*) for the Cretaceous metamorphism must represent maxima. By contrast, the Ford Granodiorite suite is likely to have retained its original fertility through the Devonian–Carboniferous metamorphism and into the Cretaceous event.

Phase equilibria modelling of the residual gneisses (Fig. 16c, d) provides information about the amount of melt left in the source after loss along the Cretaceous prograde evolution path and throughout decompression to the final solidus assemblage at *P* of 0·75–0·60 GPa and *T* of 870–830°C (Yakymchuk *et al.*, 2015*a*). The representative residual paragneiss is expected to have retained <2 vol. % melt at these *P–T* conditions, whereas the orthogneiss could have retained up to 6 vol. % melt. However, it is clear from these *P–T* pseudosections that greater

volumes of melt were potentially available at higher *P–T* conditions in the source beneath the Fosdick complex during the doming event, particularly in the orthogneiss composition.

The amount of leucosome and granite measured at outcrop in the migmatitic gneisses ranges from 40 vol. % to 70 vol. % (Yakymchuk *et al.*, 2013*b*). Thus, even if the maximum of 30 vol. % melt was generated from the Swanson Formation (Korhonen *et al*., 2010*a*) at the depth of exposure during the Cretaceous, it is likely that a significant proportion of the leucosome and granite in the Fosdick complex was sourced from deeper in the crust where ambient temperatures were higher. This is consistent with geophysical surveys across the region, which show that the crust beneath the Fosdick complex is composed of rocks similar to the Ford Granodiorite suite and the Swanson Formation (Ferraccioli *et al*., 2000; Luyendyk *et al*., 2003).

Crustal thinning associated with doming increases the apparent thermal gradient. Yakymchuk *et al.* (2013*b*) suggested that the apparent thermal gradient in the Fosdick complex prior to doming was on the order of 770°C/GPa, whereas the apparent thermal gradient that passes through *P–T* conditions for the end of doming is 1230°C/GPa (Fig. 16c, d). Extrapolating from these *P–T* conditions, it is clear that the gneisses not far beneath the Fosdick complex would have undergone a much greater degree of partial melting that could have sourced the excess leucosome and granite within the complex. At 950°C, which equates to roughly 3 km below the Fosdick complex along the 1230°C/GPa apparent thermal gradient, the paragneiss modeled would have had ~11 vol. % melt available for extraction and the orthogneiss ~20 vol. % melt (Fig. 16c, d).

The forward modelling shows that the dominant source for granite magma at depth beneath the Fosdick complex during the Cretaceous metamorphism was likely to have been the high-grade equivalents of the Ford Granodiorite suite. By contrast, magma derived from

paragneisses equivalent to the Swanson Formation would have been subordinate due to the reduced fertility after Devonian–Carboniferous metamorphism and consequent upon melt drainage during prograde heating to peak temperatures for the Cretaceous metamorphism (cf Yakymchuk & Brown, 2014).

DISCUSSION

Origin of the migmatitic gneisses

Orthogneiss

The orthogneisses have major oxide and trace element compositions that are close to those of the Ford Granodiorite suite, consistent with the hypothesis that they are the high-grade equivalents of these igneous protoliths (Figs 9, 10, 11; cf. Korhonen *et al.*, 2010*b*). Exceptions such as lower K_2O and ΣREE, and higher Al_2O_3 at low SiO_2, are consistent with modification of the composition by variable loss of granite melt and variable dissolution of accessory minerals in the source. The orthogneisses have Nd and Sr isotope compositions similar to those of the Ford Granodiorite suite at both 360 Ma (not shown) and 100 Ma (Fig. 13). Sample Y1-AW039 is an enclave of orthogneiss within Cretaceous granite that was emplaced into the thick unit of residual paragneiss at Mt Avers. Although this sample has high P_2O_5 and low Th, consistent with apatite stability during melting, the less radiogenic εNd is more likely to be the result of variable diffusive exchange with anatectic melt derived from the paragneiss prior to incorporation into the granite (cf. Lesher, 1994; Elburg, 1996). Because the zircons in the orthogneisses yield mostly Devonian–Carboniferous ages, their Hf isotope compositions were age corrected to 360 Ma. These zircons have Hf and O isotope compositions that lie within the range for zircons from the

Ford Granodiorite suite samples (Fig. 14), confirming the interpretation that the orthogneisses were derived from this protolith.

Paragneiss

The paragneisses have detrital zircon age populations that are similar to those from the Swanson Formation, consistent with the hypothesis that they are the high-grade equivalents of these metasedimentary protoliths (Yakymchuk *et al.*, 2015*b*). Furthermore, they have similar major oxide and trace element compositions (Figs 9, 10, 11). Exceptions such as higher $FeO^*+MgO+TiO_2$ and ASI at low SiO_2, and higher Th and U are consistent with modification of the composition by variable loss of granite melt and variable retention of accessory minerals in the residue. When age corrected to 100 Ma, which is the preferred age for the dominant anatectic event, all but one of the paragneiss samples have Sr and Nd isotope compositions similar to those of the Swanson Formation (Fig. 13). The exception has a more radiogenic εNd isotope compositions than the Swanson Formation, which we interpret to reflect variable diffusive exchange with anatectic melt derived from the Ford Granodiorite suite (cf. Lesher, 1994; Elburg, 1996). Considering these data in the regional context, the Swanson Formation is considered to be the likely protolith for the paragneisses in the Fosdick complex.

Petrogenesis of the granites

Granite compositions commonly depart from anatectic melt compositions generated in experimental studies. Processes that may create differences include: accessory mineral dissolution, peritectic mineral entrainment and fractional crystallization. Additional factors that may account for the variable granite compositions are source heterogeneity and blending of

melts derived from multiple sources. Below, we evaluate the relative contribution of each of these processes to the petrogenesis of granites in the Fosdick complex.

Accessory mineral dissolution

Accessory minerals may play an important role in controlling the trace element concentrations and isotope compositions of granites (e.g. Watt & Harley, 1993; Bea, 1996; Ayers & Harris, 1997; Zeng *et al*., 2005*a,b,c*). If the dissolution or growth of accessory minerals such as monazite, apatite and zircon was a dominant control on the trace element chemistry of granites then covariation is expected between various rare earth elements and P_2O_5 (apatite), Th (monazite) or Zr (zircon). As discussed above, the negative covariation between ΣLREE and P_2O_5 in the granites is consistent with apatite stability during melting. However, the weak covariation between ΣLREE and Th and the variable moderate covariation between ΣHREE and Zr suggest that crystallization and fractionation of monazite and zircon had some influence on the compositional variation (Fig. 10).

Peritectic mineral entrainment

Hydrate-breakdown melting of the deep crust is associated with the production of peritectic minerals (Brown, 2013). Some I- and S-type granite suites show covariance in major element compositions that are interpreted to represent selective entrainment of peritectic minerals from the anatectic residua (e.g. Clemens *et al.*, 2011). These minerals may be dissolved or may achieve equilibrium during melt extraction and ascent. Trends in the major element concentrations of granite suites have been attributed to varying amounts of peritectic mineral entrainment (Clemens & Stevens, 2012).

Granites from the Fosdick complex contain sparse garnet and cordierite that are usually associated with biotite-rich schlieren, which are interpreted to represent former residue entrained in the melt during extraction and, or, ascent (cf. Solar & Brown, 2001). In addition, garnet and biotite schlieren are observed locally in the smaller granite bodies and at the edges of the larger granites comprising the network of transport conduits cutting through the migmatitic gneisses. These features suggest that entrainment of peritectic garnet could have contributed to the elevated HREE patterns in some of the Cretaceous garnet-bearing granites (Fig. 12).

While outcrop observations support some peritectic mineral entrainment, it is important to evaluate if the major element chemistry of the granites in the Fosdick complex reflects this process. The relationship between source rocks and granites is evaluated using the ternary molar (Na+Ca)–(Fe*+Mg+Ti)–K diagram in Fig. 17 (Solar & Brown, 2001). Since no melting experiments have been conducted on either the Swanson Formation or the Ford Granodiorite suite, experimental melt compositions from Skjerlie *et al*. (1993), Patiño Douce & Harris (1998) and Koester *et al*. (2002) are used as analogs based on similarity in chemical composition of their starting materials to the Fosdick complex source compositions (Fig. 17). The experimental melts from Skjerlie *et al.* (1993) represent proxies for melts derived from the Ford Granodiorite suite, whereas the experimental results of Patiño Douce & Harris (1998) and Koester *et al.* (2002) represent proxies for melts derived from the Swanson Formation. These glass compositions are used to represent the melt compositions generated by anatexis of the Ford Granodiorite suite and the Swanson Formation before any modification.

None of the granites plot within the fields defined by experimental glass compositions (Fig. 17). Several granites, both garnet-absent and garnet-bearing, plot between the fields defined by the experimental glasses and may represent compositions close to unmodified crustal melts.

With the exception of one garnet-absent granite (K6-Mt38), there is no trend among the granites projecting back to either the Ford Granodiorite suite or Swanson Formation source compositions or towards garnet and, or, biotite in Fig. 17. We conclude that peritectic and, or, residual mineral entrainment was a subordinate process that may have influenced the composition of some of the garnet-bearing granites, but it was not the dominant process controlling the chemistry of granites within the Fosdick complex.

Fractional crystallization

Fractional crystallization is a scale-invariant process that can operate in large magma chambers and in individual leucosomes. Accumulation of early-crystallized feldspars through fractional crystallization and residual melt extraction has been proposed as the dominant process that controls the compositional evolution of anatectic granites (e.g. Milord & Sawyer, 1998; Solar & Brown, 2001; Morfin *et al.* 2014).

Granites from the Fosdick complex exhibit cumulate microstructures (Fig. 5) and covariation between K_2O and $CaO+Na_2O$ (Fig. 9). This covariation indicates that quartz, sodic plagioclase and K-feldspar were present on the liquidus (Morfin *et al*., 2014). Bearing in mind that the compositions of most of the granites are displaced towards the K-feldspar–plagioclase join relative to the experimental glass compositions in Fig. 17, these observations are consistent with the early accumulation of plagioclase in the less evolved magmas and K-feldspar in the more evolved magmas (cf. Morfin *et al*., 2014). The feldspar microstructures (Fig. 5), the low ΣREE contents and the moderate to large positive Eu anomalies of the granites are consistent with a cumulate origin for many of them.

By projecting from a likely melt composition through each sample onto the K-feldspar–plagioclase edge in the molar (Na+Ca)–(Fe*+Mg+Ti)–K diagram (Fig. 17), an estimate may be made of the amount and mode of cumulate material present in each granite (Solar & Brown, 2001; Korhonen *et al.*, 2010b). The cumulate proportions were evaluated relative to the glass compositions from the experiments of Skjerlie *et al*. (1993). Using this method, the Cretaceous granites comprise 30% to 90% cumulate material composed of variable proportions of K-feldspar (dominant) and plagioclase (subordinate). As pointed out by Morfin *et al*. (2014), the dominance of K-feldspar indicates that the melts were sufficiently evolved due to early plagioclase fractionation in the source that they were able to crystallize K-feldspar at the level of emplacement. Thus, the melts are inferred to have been derived from deeper in the crust.

Several granites, both garnet-absent and garnet-bearing, plot between the fields defined by experimental glasses and may represent compositions close to unmodified crustal melts. These granites also plot in the centre of the array of granite compositions in the plot of K_2O vs $CaO+Na_2O$ (Fig. 9), and two garnet-absent granites from this group (C5-R23 and C5-Is54) have the highest ΣREE concentrations and only small negative Eu anomalies (Fig. 12). The most plagioclase rich granite (Y1-AE051) plots at the low K_2O end of the granite array in the plot of K_2O vs $CaO+Na_2O$, whereas the most K-feldspar rich granite (Y1-AW038) plots at the high K_2O end of the array (Fig. 9). Since the granites exhibit early-crystallized feldspar (Fig. 5), they cannot be related by simple fractional crystallization and separation of cumulate minerals from evolved melt. It is more likely that the individual samples of granite represent the cumulate products derived from a variably fractionated melt. Thus, each batch of melt that migrated through the Fosdick complex followed its own fractional crystallization trend, as might be expected from episodic drainage of melt from the suprasolidus crust. Thus, this study adds to the

growing body of data supporting the progressive construction of injection complexes and granite plutons (Brown, 2013; Yakymchuk *et al*., 2013*b*; Morfin *et al*., 2013, 2014).

The fractional crystallization model may be evaluated further using the large-ion lithophile elements, as shown in Fig. 18. In Fig. 18, the effects of fractional crystallization of plagioclase, K-feldspar and biotite are shown for two representative starting melt compositions with Rb, Sr and Ba concentrations of 120 or 400 ppm, 75 or 400 ppm and 100 or 800 ppm, and Rb/Sr ratios of 1 or 2, respectively. Fractional crystallization is modeled using the average of the partition coefficients reported by Nash & Crecraft (1985). For the Cretaceous granites from inside the Fosdick complex, biotite does not play a significant role, and the trends in the data are reproduced satisfactorily by accumulation of dominantly K-feldspar, with only a subordinate role for plagioclase (Fig. 18). Therefore, fractional crystallization appears to have been the major process that controlled the major and trace element concentrations of anatectic granites in the Fosdick complex.

Source heterogeneity

Chemical and isotopic heterogeneity of source rocks can produce granites with variable compositions (e.g. Hill *et al.*, 1986; Deniel *et al.*, 1987; Pressley & Brown, 1999; Villaros *et al.*, 2012). Both the Swanson Formation and the Ford Granodiorite suite exhibit significant elemental and isotopic heterogeneity. Consequently, extraction of multiple batches of melt generated during anatexis of these sources is also expected to result in significant elemental and isotope heterogeneity. However, if the isotope composition of the granites falls within the range of values for the putative source rocks, then it is reasonable to posit that they were derived from

such a source. Next we evaluate the petrogenetic relationship between the anatectic granites and their putative sources in the Fosdick complex using Sr, Nd, Hf and O isotopes.

Figure 13 shows that the Cretaceous granites have whole-rock Sr and Nd isotope compositions that extend from those typical of the Ford Granodiorite suite and the orthogneisses towards values typical for the Swanson Formation and the paragneisses. This suggests that the granites represent variable combinations of melts derived from both sources. One of the garnet-absent granites (C6-AW86-1) was originally argued to be part of the Devonian–Carboniferous suite (Siddoway & Fanning, 2009), but the presence of Cretaceous zircons and its geochemical characteristics indicate that it is likely to be Cretaceous in age.

In Fig. 15 the εHf values of detrital zircons in the Swanson Formation are recalculated to 100 Ma. The εHf_{100} values of these zircons vary from -3 to -73, with a median value of -17·5 and an interquartile range of -13·9 to -30·3. The $\delta^{18}O$ value of zircons that crystallized from melt produced from the Swanson Formation are expected be ~8·5–12·0‰, with a mean value of 10·5‰ (Yakymchuk *et al*., 2015b). Figure 16 shows that Hf and O isotope data for zircons from samples Y1-IG070, Y1-AW038 and C6-AW86-1 plot within the field defined by the Ford Granodiorite suite, albeit in the sector with more radiogenic εHf_{100} values and higher $\delta^{18}O$ values.

Samples Y1-IG070 and Y1-AW038 have a similar range and mean of εHf_{100} and $\delta^{18}O$ values. In addition, both samples have $^{87}Sr/^{86}Sr$ ratios (recalculated to 100Ma) that overlap within uncertainty, but sample Y1-IG070 has an εNd_{100} value of -7·5 whereas sample Y1-AW038 has a more radiogenic value of -5·5 (Fig. 13). This suggests decoupling of the Nd isotope systematics from the other isotope systems for sample Y1-IG070. Since both granites have similar very low P_2O_5 and ΣREE, and Th is below detection, decoupling is unlikely to be due to accessory mineral behavior in the source. We speculate that this difference might be due

to variable diffusive exchange of Sm and Nd between anatectic melt derived from a Ford Granodiorite suite source and the Swanson Formation during melt transport and emplacement. In contrast, although zircons from sample Y1-IG062 have a similar range of εHf_{100} values to the other two granites, many plot at values of $\delta^{18}O$ slightly above the Ford Granodiorite suite field (Fig. 15b). Nonetheless, the Hf and O isotope values of zircon from this sample are within uncertainty of the field defined by values from the Ford Granodiorite suite. Based on the Hf and O isotope data, it is permissible that all three granites were derived from this source.

However, the Sr and Nd isotope data suggest some contribution of melt from the Swanson Formation to the granites (Fig. 13). Considering the large Hf and O isotope heterogeneity of the Ford Granodiorite suite, we cannot exclude the possibility that the granites were sourced from a juvenile member of the Ford Granodiorite suite that mixed with melt derived from the Swanson Formation. This hypothesis is evaluated in the next section.

Magma mixing

More than two thirds of the granites analyzed from the Fosdick complex have Sr and Nd isotope values that lie between those of the two putative sources. To evaluate the relative contribution of these sources to the final composition of the granites, binary mixing lines were calculated using the Sr and Nd concentrations and calculated initial ratios of more and less radiogenic end-members of the Swanson Formation and the Ford Granodiorite suite (Fig. 13). These binary mixing lines also enclose the Sr and Nd isotope values for most of the orthogneisses and paragneisses (Fig. 13). For four of the Cretaceous granites, the Sr and Nd isotope compositions are consistent with being derived solely from a source similar to the Ford Granodiorite suite,

whereas the Sr and Nd isotope compositions of the remainder allow a contribution of up to 40% melt derived from a source similar to the Swanson Formation.

Limits may also be placed on the amount of Swanson Formation (or paragneiss) that might have been involved in the petrogenesis of these granites using the εHf_{100} and $\delta^{18}O$ zircon data discussed above. To account for source heterogeneity, Fig. 15b shows binary mixing lines that connect representative end-member compositions for the Swanson Formation and the Ford Granodiorite suite. Two scenarios are modeled, one in which anatectic melt derived from the Ford Granodiorite suite is mixed with anatectic melt derived from the Swanson Formation, and another in which it is mixed with Swanson Formation *en masse* by assimilation. The curvature of the mixing lines is most sensitive to the relative concentrations of Hf in each of the end-members. For the Swanson Formation, an average whole-rock concentration of 3·2 ppm Hf was assigned, based on bulk chemical analyses (Korhonen *et al.*, 2010*a*). For anatectic melt derived from the Swanson Formation or the Ford Granodiorite suite, a concentration of 1·0 ppm is used (e.g. Yakymchuk *et al.*, 2013*a*). Within uncertainty, zircons from the Cretaceous granites plot in the field bounded by the two mixing lines. If anatectic melt derived from the Ford Granodiorite suite mixed with anatectic melt derived from the Swanson Formation, then the maximum contribution from the latter is 30% (Fig. 15b). By contrast, for *en masse* assimilation of the Swanson Formation, the limit is 10% (Fig. 15b).

In the above model no juvenile input is required. However, a juvenile input cannot be ruled out by the isotope data alone, since blending melts from an appropriate mantle source and an upper crustal source similar to the Swanson Formation will also yield compositions that enclose the data shown in Fig. 15, as discussed for Devonian–Carboniferous granites in the Fosdick complex by Yakymchuk *et al.* (2015*b*). However, since there is no evidence of any

juvenile input, the parsimonious interpretation favours derivation of the granites from the putative crustal sources. Furthermore, the inferences from the Sr, Nd, Hf and O isotope data, which require a larger component derived from a source similar to the Ford Granodiorite suite and a smaller component derived from a source similar to the Swanson Formation, are consistent with the predictions about melt sources based on the phase equilibria modeling discussed earlier (Fig. 16).

Cumulate granites in migmatitic gneiss domes

The variable major oxide and trace element chemistry (Figs 9 & 10), relatively low Rb/Sr ratios, dominance of pronounced positive Eu anomalies (Fig. 12) and location close to the K-feldspar–plagioclase edge of the molar (Na+Ca)–(Fe*+Mg+Ti)–K diagram (Fig. 17) for many of the granites are features consistent with fractional crystallization and accumulation of feldspar. Granites forming sub-horizontal sheets and discordant networks in the Fosdick complex commonly contain coarse euhedral feldspars, consistent with a cumulate origin. However, the covariation between K_2O and $CaO+Na_2O$ for these granites indicates fractionation of feldspar during transport from the source prior to entrapment at their present structural level within the complex. This process may involve continuous separation of feldspar from the evolving liquid in the manner proposed by Morfin *et al.* (2014), and might be the mechanism that operated in the granite networks within the deeper crust of the Fosdick complex. However, after entrapment, melt drainage from the crystallizing granites within the Fosdick complex appears to have been related to dome formation, particularly in the sheeted leucogranite complex immediately below the South Fosdick detachment system. These granites are interpreted to record the collapse of sub-horizontal partially crystallized layers of magma by filter pressing (e.g. Brown *et al.*, 1995)

during vertical shortening associated with normal-sense displacement across the South Fosdick detachment system and dome exhumation, leaving behind cumulate-rich residues. The evolved melt likely drained to shallow crustal levels and the resulting granites may have been lost to erosion. Some of this evolved melt may be preserved in the Byrd Coast granite suite, as discussed by Korhonen *et al.* (2010*b*).

The Cretaceous granites in the Fosdick complex crystallized between 115 and 100 Ma, with a dominant grouping at 107–100 Ma (Fig. 19). Syntectonic granites in the South Fosdick detachment zone yield U–Pb zircon ages of 109–102 Ma (McFadden *et al*., 2010a). This time frame corresponds to a period of transition in regional tectonics from oblique convergence to oblique extension that facilitated dome formation and exhumation of the complex (Siddoway, 2005, 2008; McFadden *et al.*, 2010*a*, *b*). Exhumation was likely a fast process. The full set of geochronological data now available for the complex is compiled in Fig. 19, from which it is clear that the main period of granite crystallization (107–100 Ma) coincides with the younger period of emplacement of mafic dykes during lithosphere extension (Saito *et al*., 2013). In addition, these granite ages overlap the younger part of the range of U–Pb metamorphic ages retrieved from monazite, the post-peak Sm-Nd ages retrieved from garnet, and the $^{40}Ar/^{39}Ar$ ages retrieved from hornblende (Fig. 19). These concordent ages suggest rapid cooling and exhumation of the Fosdick complex at *c.* 100 Ma. Dome formation and exhumation of the middle crust is confirmed by the correspondence between crystallization ages of the younger mafic dykes and the $^{40}Ar/^{39}Ar$ ages retrieved from biotite, muscovite and K-feldspar (Fig. 19).

The results of this study contribute to a growing body of work which suggests that leucosomes in migmatites and associated granites represent accumulations of feldspar and do not reflect primary crustal melt compositions (e.g. Cuney & Barbey, 1982; Sawyer, 1987; Milord *et*

al., 2001; Solar & Brown, 2001; Johannes *et al.*, 2003; Korhonen *et al.*, 2010*b*; Morfin *et al.*, 2014). There are two important implications if granites in migmatitic gneiss domes are typically cumulate. First, it is possible that the accumulation of early-crystallized minerals in magma transport conduits may restrict the flow of melt and even locally choke the plumbing system. This possibility may need to be considered as a rate-limiting step in estimating the timescales of melt extraction from the deep crust. Second, the drained melt is likely to have a more evolved composition than that represented by melt inclusions in migmatites and, in particular, it is likely to have higher concentrations of the heat-producing elements. This will have important implications for the tectonic history of large hot mountain belts (Jamieson *et al.*, 2011), cooling ultrahigh-temperature (UHT) metamorphic terranes (Korhonen *et al*., 2013), priming the crust for future UHT metamorphic events (Brown & Korhonen, 2009; Clark *et al.*, 2011), the particular style of some Proterozoic 'hot' orogens (McLaren & Powell, 2014), and the long-term stability of the continental crust (Sandiford & McLaren, 2002).

CONCLUSIONS

In the Fosdick migmatite–granite complex of Marie Byrd Land in West Antarctica, Cretaceous granites have Sr, Nd, Hf and O isotope compositions consistent with derivation from regional sources that display significant isotope heterogeneity. The major oxide and trace element concentrations of the granites are highly variable; they reflect fractional crystallization and the accumulation of early-crystallized feldspar during magma ascent and emplacement. This conclusion is supported by the cumulate microstructures, low ΣREE contents and common positive Eu anomalies that characterize the Cretaceous granites in the Fosdick complex.

Peritectic mineral entrainment and accessory mineral dissolution, entrainment and crystallization exerted only minimal influence on the elemental variation of these granites.

In a wider context, granites in migmatite complexes typically do not represent melt compositions; they are more likely to be cumulates left after melt drainage. Thus, the amount of granite hosted within migmatitic crust cannot be used as an estimate of melt volume present at any time during the suprasolidus evolution. Conversely, granites that have crystallized at shallower levels in the crust are more likely to represent the complementary fractionated melts with evolved compositions.

FUNDING

This work was supported by the US National Science Foundation [ANT0944615 to MB], [OPP-0338279, OPP-0944600 to CS], and [EAR1032156 to Arizona LaserChron Center], the NISPLab at the University of Maryland, and the Geological Society of America [Graduate Research Grant to CB]. CY was partially funded by a Post-Graduate scholarship and Discovery Grant from the National Science and Engineering Research Council of Canada

SUPPLEMENTARY DATA

Results of U–Pb zircon geochronology are presented in Supplementary Electronic Appendix Tables 1 and 2.

ACKNOWLEDGEMENTS

The authors acknowledge use of facilities in the NanoCenter and the NISP-Lab at the University of Maryland, which is a MRSEC Shared Experimental Facility. The authors thank Richard Ash (Plasma Mass Spectrometry Laboratory) and Igor Puchtel and Richard Walker (Isotope Geochemistry Laboratory) at the University of Maryland for help and guidance with analysis, M.

Pecha and M. Ibanez-Mejia for assistance with data collection at the Arizona LaserChron Center (supported by the National Science Foundation under Grant No. EAR1032156), Bin Fu for assistance with sample preparation and analysis at the Australian National University, T. Burton, K. Emery and D. Uhlmann for field logistics and safety, and Kenn Borek Air and Raytheon Polar Services personnel for transportation and logistical support. We thank H. Stowell, F. Farina, E. Sawyer and two anonymous reviewers for thorough and constructive comments and Jim Beard for editorial comments and advice.

REFERENCES

Acosta-Vigil, A., Cesare, B., London, D. & Morgan Vi, G. B. (2007). Microstructures and composition of melt inclusions in a crustal anatectic environment, represented by metapelitic enclaves within El Hoyazo dacites, SE Spain. *Chemical Geology* **237**, 450–465.

Adams, C. J. (1986). Geochronological studies of the Swanson Formation of Marie Byrd Land, West Antarctica, and correlation with northern Victoria Land, East Antarctica, and South Island, New Zealand. *New Zealand Journal of Geology and Geophysics,* **29**, 345–358

Adams, C. J. (1987). Geochronology of granite terranes in the Ford Ranges, Marie Byrd Land, West Antarctica. *New Zealand Journal of Geology and Geophysics,* **30**, 54–72.

Ayres, M. & Harris, N. (1997). REE fractionation and Nd-isotope disequilibrium during crustal anatexis: constraints from Himalayan leucogranites. *Chemical Geology* **139**, 249–269.

Bartoli, O., Cesare, B., Poli, S., Bodnar, R. J., Acosta-Vigil, A., Frezzotti, M. L. & Meli, S. (2013). Recovering the composition of melt and the fluid regime at the onset of crustal anatexis and S-type granite formation. *Geology* **41**, 115–118.

Bea, F. (1996). Residence of REE, Y, Th and U in granites and crustal protoliths; implications for the chemistry of crustal melts. *Journal of Petrology* **37**, 521–552.

Black, L. P., Kamo, S. L., Allen, C. M., Aleinikoff, J. N., Davis, D. W., Korsch, R. J. & Foudoulis, C. (2003). TEMORA 1: a new zircon standard for Phanerozoic U–Pb geochronology. *Chemical Geology* **200**, 155-170.

Boyd, F. R. & Mertzmann, S. (1987). Composition and structure of the Kaapvaal lithosphere, Southern Africa. In: Mysen, B. O. (ed.) *Magmatic Processes: Physiochemical Principles*, 13–24.

Brown, M., Averkin, Y.A., McLellan, E.L. & Sawyer, E.W. (1995). Melt segregation in migmatites. *Journal of Geophysical Research*, **100**, 15655–15679

Brown, M. (2010). Melting of the continental crust during orogenesis: the thermal, rheological, and compositional consequences of melt transport from lower to upper continental crust. *Canadian Journal of Earth Sciences* **47**, 655-694.

Brown, M., 2013. Granite: from genesis to emplacement. Geological Society of America Bulletin, 125, 1079–1113.

Brown, M.A., Brown, M., Carlson, W.D. & Denison, C. (1999). Topology of syntectonic melt flow networks in the deep crust: inferences from three-dimensional images of leucosome geometry in migmatites. *American Mineralogist*, **84**, 1793–1818.

Brown, M. & Korhonen, F.J. (2009). Some remarks on melting and extreme metamorphism of crustal rocks. In: Dasgupta, S. (ed.) *Physics and Chemistry of the Earth.* Published for the Indian National Science Academy by Springer, New York, 67–87.

Cesare, B., Maineri, C., Baron Toaldo, A., Pedron, D. & Acosta Vigil, A. (2007). Immiscibility between carbonic fluids and granitic melts during crustal anatexis: A fluid and melt inclusion study in the enclaves of the Neogene Volcanic Province of SE Spain. *Chemical geology* **237**, 433–449.

Clark, C., Fitzsimons, I. C., Healy, D. & Harley, S. L. (2011). How does the continental crust get really hot? *Elements* **7**, 235–240.

Clemens, J. D., Stevens, G., Farina, F. (2011). The enigmatic sources of I-type granites: The peritectic connexion. *Lithos* **126**, 174–181.

Clemens, J.D. & Stevens G. (2012). What controls chemical variation in granitic magmas? *Lithos* **134–135**, 317–329.

Coggon, R. & Holland, T. J. B. (2002). Mixing properties of phengitic micas and revised garnet-phengite thermobarometers. *Journal of Metamorphic Geology* **20**, 683-696.

Cuney, M. & Barbey, P. (1982). Mise en evidence de phenomenes de cristallisation fractionnee dans les migmatites. *Comptes-Rendus des Seances de L'Academie des Sciences, Serie* **2**, 37–42.

Deniel, C., Vidal, P., Fernandez, A., Le Fort, P., Peucat, J.-J. (1987). Isotopic study of the Manaslu granite (Himalaya, Nepal): inferences on the age and source of Himalayan leucogranites. *Contributions to Mineralogy and Petrology* **96**, 78-92.

Diener, J. F. A., Powell, R., White, R. W., Holland, T. J. B. (2007). A new thermodynamic model for clino- and orthoamphiboles in the system Na2O–CaO–FeO–MgO–Al2O3–SiO2–H2O–O. *Journal of Metamorphic Geology* **25**, 631-656.

Diener, J. F. A., White, R. W., Powell, R. (2008). Granulite facies metamorphism and subsolidus fluid-absent reworking, Strangways Range, Arunta Block, central Australia. *Journal of Metamorphic Geology* **26**, 603-622.

Elburg, M.A. (1996). Evidence of isotopic equilibration between microgranitoid enclaves and host granodiorite,Warburton Granodiorite, Lachlan Fold Belt, Australia. *Lithos*, **38**, 1–22.

Ferraccioli, F., Bozzo, E. & Damaske, D. (2002). Aeromagnetic signatures over western Marie Byrd Land provide insight into magmatic arc basement, mafic magmatism and structure of the Eastern Ross Sea Rift flank. *Tectonophysics* **347**, 139–165.

Ferrero, S., Bartoli, O., Cesare, B., Salvioli-Mariani, E., Acosta-Vigil, A., Cavallo, A., Groppo, C. & Battiston, S. (2012). Microstructures of melt inclusions in anatectic metasedimentary rocks. *Journal of Metamorphic Geology* **30**, 303–322.

Ferrero, S., Bodnar, R. J., Cesare, B. & Viti, C. (2011). Re-equilibration of primary fluid inclusions in peritectic garnet from metapelitic enclaves, El Hoyazo, Spain. *Lithos* **124**, 117–131.

Ferrero, S., Braga, R., Berkesi, M., Cesare, B. & Laridhi Ouazaa, N. (2014). Production of metaluminous melt during fluid-present anatexis: an example from the Maghrebian basement, La Galite Archipelago, central Mediterranean. *Journal of Metamorphic Geology* **32**, 209–225.

Gehrels, G. E., Valencia, V. A. & Ruiz, J. (2008). Enhanced precision, accuracy, efficiency, and spatial resolution of U-Pb ages by laser ablation–multicollector–inductively coupled plasma–mass spectrometry. *Geochemistry, Geophysics, Geosystems* **9**, Q03017.

Green, E., Holland, T., Powell, R. (2007). An order-disorder model for omphacitic pyroxenes in the system jadeite-diopside-hedenbergite-acmite, with applications to eclogitic rocks. *American Mineralogist* **92**, 1181-1189.

Hill, R. I., Silver, L. T., Taylor, H. P., Jr. (1986). Coupled Sr-O isotope variations as an indicator of source heterogeneity for the Northern peninsular ranges batholith. *Contributions to Mineralogy and Petrology* **92**, 351-361.

Holland, T. J. B. & Powell, R. (1998). An internally consistent thermodynamic data set for phases of petrological interest. *Journal of Metamorphic Geology* **16**, 309–343.

Holland, T. & Powell, R. (2003). Activity–composition relations for phases in petrological calculations: an asymmetric multicomponent formulation. *Contributions to Mineralogy and Petrology* **145**, 492-501.

Ickert, R. B., Hiess, J., Williams, I. S., Holden, P., Ireland, T. R., Lanc, P., Schram, N., Foster, J. J. & Clement, S. W. (2008). Determining high precision, in situ, oxygen isotope ratios with a SHRIMP II: Analyses of MPI-DING silicate-glass reference materials and zircon from contrasting granites. *Chemical geology* **257**, 114-128.

Jamieson, R. A., Unsworth, M. J., Harris, N. B. W., Rosenberg, C. L. & Schulmann, K. (2011). Crustal Melting and the Flow of Mountains. *Elements* **7**, 253–260.

Johannes, W., Ehlers, C., Kriegsman, L. M. & Mengel, K. (2003). The link between migmatites and S-type granites in the Turku area, southern Finland. *Lithos* **68**, 69–90.

Kemp, A. I. S., Hawkesworth, C. J., Foster, G. L., Paterson, B. A., Woodhead, J. D., Hergt, J. M., Gray, C. M., Whitehouse, M. J. (2007). Magmatic and Crustal Differentiation History of Granitic Rocks from Hf-O Isotopes in Zircon. *Science* **315**, 980–983.

Koester, E., Pawley, A.R., Fernandes, L.A.D., Porcher, C.C. & Soiani, E. (2002). Experimental melting of cordieite gneiss and the petrogenesis of syntranscurrent peraluminous granites in southern Brazil. *Journal of Petrology*, **43**, 1595–1616.

Korhonen, F. J., Saito, S., Brown, M. & Siddoway, C. S. (2010*a*). Modelling multiple melt loss events in the evolution of an active continental margin. *Lithos*, **116**, 230–248.

Korhonen, F. J., Saito, S., Brown, M., Siddoway, C. S. & Day, J. M. D. (2010*b*). Multiple Generations of Granite in the Fosdick Mountains, Marie Byrd Land, West Antarctica: Implications for Polyphase Intracrustal Differentiation in a Continental Margin Setting. *Journal of Petrology*, **51**, 627–670.

Korhonen, F. J., Brown, M., Grove, M., Siddoway, C. S., Baxter, E. F. & Inglis, J. D. (2012). Separating metamorphic events in the Fosdick migmatite–granite complex, West Antarctica. *Journal of Metamorphic Geology*, **30**, 165–192.

Korhonen, F. J., Clark, C., Brown, M., Bhattacharya, S. & Taylor, R. (2013). How long-lived is ultrahigh temperature (UHT) metamorphism? Constraints from zircon and monazite geochronology in the Eastern Ghats orogenic belt, India. *Precambrian Research* **234**, 322–350.

Lesher, C.E. (1994). Kinetics of Sr and Nd exchange in silicate liquids: Theory, experiments, and applications to uphill diffusion, isotopic equilibration, and irreversible mixing of magmas. *Journal of Geophysical Research*, **99**, 9585–9604.

Ludwig, K. R. (2001). User's guide to SQUID 2.2. Berkeley: Berkeley Geochronology Center.

Ludwig, K. R. (2003). User's manual for ISOPLOT 3, A Geochronological Toolkt for Microsoft Excel. Berkeley: Berkeley Geochronology Center, Special Publication No. 4.

Luyendyk, B. P., Wilson, D. S. & Siddoway, C. S. (2003). Eastern margin of the Ross Sea Rift in western Marie Byrd Land, Antarctica: Crustal structure and tectonic development. *Geochemistry, Geophysics, Geosystems* **4**, 1090.

McDonough, W.F. & Sun, S-s. (1995). The composition of the Earth. *Chemical Geology*, **120**, 223–254.

McFadden, R.R., Siddoway, C.S, Teyssier, C. & Fanning, C.M. (2010*a*). Cretaceous oblique extensional deformation and magma accumulation in the Fosdick Mountains migmatite-cored gneiss dome, West Antarctica. *Tectonics*, **29**, TC4022.

McFadden. R.R., Teyssier, C., Siddoway, C.S., Whitney, D.L. & Fanning, C.M. (2010*b*). Oblique dilation, melt transfer, and gneiss dome emplacement. *Geology,* **38**, 375–378.

McLaren, S. & Powell, R. (2014). Magmatism, orogeny and the origin of high-heat-producing granites in Australian Proterozoic terranes. Journal of the Geological Society, London, 171, 149–152.

Milord, I., Sawyer, E.W., Brown, M. (2001). Formation of diatexite migmatite and granite magma during anatexis of semi-pelitic metasedimentary rocks: an example from St. Malo, France. *Journal of Petrology*, **42**, 487–505.

Morfin, S., Sawyer, E. W. & Bandyayera, D. (2013). Large volumes of anatectic melt retained in granulite facies migmatites: An injection complex in northern Quebec. *Lithos* **168–169**, 200–218.

Morfin, S., Sawyer, E.W. & Bandyayera, D. (2014). The geochemical signature of a felsic injection complex in the continental crust: Opinaca Subprovince, Quebe. *Lithos*, **196–197**, 339–355.

Mukasa, S.B. & Dalziel, I.W.D. (2000). Marie Byrd Land, West Antarctica: Evolution of Gondwana's Pacific margin constrained by zircon U-Pb geochronology and feldspar common-Pb isotopic compositions. *GSA Bulletin*, **112**, 611–627.

Munizaga, F., Maksaev, V., Fanning, C. M., Giglio, S., Yaxley, G. & Tassinari, C. C. G. (2008). Late Paleozoic,ÄìEarly Triassic magmatism on the western margin of Gondwana: Collahuasi area, Northern Chile. *Gondwana Research* **13**, 407-427.

Nash, W.P. & Crecraft, H.R. (1985). Partition coefficients for trace elements in silicic magmas. *Geochimica et Cosmochimica Acta*, **49**, 2309–2322.

Norton, D. & Taylor, H. P. (1979). Quantitative Simulation of the Hydrothermal Systems of Crystallizing Magmas on the Basis of Transport Theory and Oxygen Isotope Data: An analysis of the Skaergaard Intrusion. *Journal of Petrology* **20**, 421–486.

Pankhurst, R.J., Weaver, S.D., Bradshaw, J.D., Storey, B.C. & Ireland, T.R. (1998). Geochronology and geochemistry of pre-Jurassic superterranes in Marie Byrd Land, Antarctica. *Journal of Geophysical Research*, **103**, 2529–2547.

Patiño Douce, A. E. & Harris, N. B. W. (1998). Experimental Constraints on Himalayan Anatexis. *Journal of Petrology*, **39**, 689–710.

Powell, R. & Holland, T. J. B. (1988). An internally consistent dataset with uncertainties and correlations: 3. Applications to geobarometry, worked examples and a computer program. *Journal of Metamorphic Geology* **6**, 173–204.

Pressley, R. A. & Brown, M. (1999). The Phillips pluton, Maine, USA: evidence of heterogeneous crustal sources and implications for granite ascent and emplacement mechanisms in convergent orogens. *Lithos* **46**, 335-366.

Richard, S.M., Smith, C.H., Kimbrough, D.L., Fitzgerald, P.G., Luyendyk, B.P. & McWilliams, M.O. (1994). Cooling history of the northern Ford Ranges, Marie Byrd Land, West Antarctica. *Tectonics,* **13**, 837–857.

Rosenberg, C. L. & Handy, M. R. (2005). Experimental deformation of partially melted granite revisited: implications for the continental crust. *Journal of Metamorphic Geology* **23**, 19–28.

Saito, S., Brown, M., Korhonen, F.J., McFadden, R.R. & Siddoway, C.S. (2013). Petrogenesis of Cretaceous mafic intrusive rocks, Fosdick Mountains, West Antarctica: Melting of the sub-continental arc mantle along the Gondwana margin. *Gondwana Research*, **23**, 1567–1580.

Sambridge, M. S. & Compston, W. (1994). Mixture modeling of multi-component data sets with application to ion-probe zircon ages. *Earth and Planetary Science Letters* **128**, 373–390.

Sandiford, M. & McLaren, S. (2002). Tectonic feedback and the ordering of heat producing elements within the continental lithosphere. *Earth and Planetary Science Letters*, **204**, 133–150.

Sawyer, E. W. (1987). The Role of Partial Melting and Fractional Crystallization in Determining Discordant Migmatite Leucosome Compositions. *Journal of Petrology* **28**, 445–473.

Sawyer, E. (1991). Disequilibrium melting and the rate of melt–residuum separation during migmatization of mafic rocks from the Grenville Front, Quebec. *Journal of Petrology* **32**, 701–738.

Sawyer, E.W., Cesare, B. & Brown, M. (2011). When the Continental Crust Melts. *Elements*, **7**, 229–234

Scherer, E., Münker, C. & Mezger, K. (2001). Calibration of the Lutetium-Hafnium Clock. *Science* **293**, 683–687.

Siddoway, C. (2008). Tectonics of the West Antarctic Rift System: new light on the history and dynamics of distributed intracontinental extension. In: Cooper, A. K., Barrett, P. J., Stagg, H., Storey, B., Stump, E. & Wise, W. (eds.) *Antarctica: A Keystone in a Changing World*. Washington D.C.: National Academies Press, 91–114.

Siddoway, C.S. & Fanning, C.M. (2009). Paleozoic tectonism on the East Gondwana margin: Evidence from SHRIMP U–Pb zircon geochronology of a migmatite–granite complex in West Antarctica. *Tectonophysics*, **477**, 262–277.

Siddoway, C.S., Richard, S.M., Fanning, C.M. & Luyendyk, B.P. (2004). Origin and emplacement of a middle Cretaceous gneiss dome, Fosdick Mountains, West Antarctica, in Whitney, D.L., et al., eds., Gneiss domes in orogeny*: Geological Society of America Special Paper*, **380**, 267–294

Siddoway, C.S., Sass, L.C., III & Esser, R. (2005). Kinematic history of Marie Byrd Land terrane, West Antarctica: Direct evidence from Cretaceous mafic dykes, in Vaughan, A.P.M., et al., eds., Terrane processes at the margin of Gondwana: *Geological Society of London Special Publication*, **246**, 417–438.

Skjerlie, K.P., Patiño Douce, A.E. & Johnston, A.D. (1993). Fluid absent melting of a layered crustal protolith: implications for the generation of anatectic granites. *Contributions to Mineralogy and Petrology,* **114**, 365–378.

Solar, G.S. & Brown, M. (2001). Petrogenesis of migmatites in Maine, USA: Possible source of peraluminous leucogranite in plutons? *Journal of Petrology*, **42**, 789–823.

Taylor, J. & Stevens, G. (2010). Selective entrainment of peritectic garnet into S-type granitic magmas Evidence from Archaean mid-crustal anatectites. *Lithos*, **120**, 277–292.

Tera, F. & Wasserburg, G. J. (1972). U-Th-Pb systematics in three Apollo 14 basalts and the problem of initial Pb in lunar rocks. *Earth and Planetary Science Letters* **14**, 281–304.

Tulloch, A.J., Ramezani, J., Kimbrough, D.L., Faure, K. & Allibone, A.H. (2009*a*). U–Pb geochronology of mid-Paleozoic plutonism in western New Zealand: Implications for S-type granite generation and growth of the east Gondwana margin. *Geological Society of America Bulletin*, **121**, 1236–1261.

Tulloch, A. J., Ramezani, J., Mortimer, N., Mortensen, J., van den Bogaard, P. & Maas, R. (2009*b*). Cretaceous felsic volcanism in New Zealand and Lord Howe Rise (Zealandia) as a precursor to final Gondwana break-up. *Geological Society, London, Special Publications* **321**, 89–118.

Valley, J. W., Kinny, P. D., Schulze, D. J. & Spicuzza, M. J. (1998). Zircon megacrysts from kimberlite: oxygen isotope variability among mantle melts. *Contributions to Mineralogy and Petrology* **133**, 1–11.

Veevers, J. J. (2012). Reconstructions before rifting and drifting reveal the geological connections between Antarctica and its conjugates in Gondwanaland. *Earth-Science Reviews* **111**, 249–318.

Villaros, A., Stevens, G., Moyen, J.-F. & Buick, I. (2009). The trace element compositions of S-type granites: evidence for disequilibrium melting and accessory phase entrainment in the source. *Contributions to Mineralogy and Petrology* **158**, 543–561.

Villaros, A., Buick, I. S., Stevens, G. (2012). Isotopic variations in S-type granites: an inheritance from a heterogeneous source? *Contributions to Mineralogy and Petrology* **163**, 243-257.

Watt, G. R. & Harley, S. L. (1993). Accessory phase controls on the geochemistry of crustal melts and restites produced during water-undersaturated partial melting. *Contributions to Mineralogy and Petrology* **114**, 550–566.

Weaver, S.D., Bradshaw, J.D. & Adams, C.J. (1991). Granitoids of the Ford Ranges, Marie Byrd, Land, Antarctica. In: Geological Evolution of Antarctica (eds Thompson, M.R.A., Grame, J.A. and Thompson, J.W.), pp. 345–351, Cambridge University Press, Cambridge.

Weaver, S. D., Adams, C. J., Pankhurst, R. J. & Gibson, I. L. (1992). Granites of Edward VII Peninsula, Marie Byrd Land: anorogenic magmatism related to Antarctic–New Zealand rifting. *Transactions of the Royal Society of Edinburgh: Earth Sciences*, **83**, 281–290.

Weaver, S.D., Storey, B.C., Pankhurst, R. J., Mukasa, S.B., DiVenere, V.J. & Bradshaw, J.D., 1994. Antarctica-New Zealand rifting and Marie Byrd Land lithospheric magmatism linked to ridge subduction and mantle plume activity. Geology, 22, 811–814.

White, R. W. & Powell, R. (2002). Melt loss and the preservation of granulite facies mineral assemblages. *Journal of Metamorphic Geology* **20**, 621-632.

White, Powell, Holland, Worley. (2000). The effect of TiO2 and Fe2O3 on metapelitic assemblages at greenschist and amphibolite facies conditions: mineral equilibria calculations in the system K2O–FeO–MgO–Al2O3–SiO2–H2O–TiO2–Fe2O3. *Journal of Metamorphic Geology* **18**, 497–511.

White, R. W., Powell, R., Halpin, J. A. (2004). Spatially-focussed melt formation in aluminous metapelites from Broken Hill, Australia. *Journal of Metamorphic Geology* **22**, 825–845.

White, R. W., Pomroy, N. E., Powell, R. (2005). An in situ metatexite–diatexite transition in upper amphibolite facies rocks from Broken Hill, Australia. *Journal of Metamorphic Geology* **23**, 579-602.

White, R. W., Powell, R., Holland, T. J. B. (2007). Progress relating to calculation of partial melting equilibria for metapelites. *Journal of Metamorphic Geology* **25**, 511-527.

White, R. W., Stevens, G. & Johnson, T. E. (2011). Is the Crucible Reproducible? Reconciling Melting Experiments with Thermodynamic Calculations. *Elements* **7**, 241–246.

Williams, I. S. (1998). U–Th–Pb geochronology by ion microprobe. *Applications of microanalytical techniques to understanding mineralizing processes*, 1–25.

Woodhead, J., Hergt, J., Shelley, M., Eggins, S. & Kemp, R. (2004). Zircon Hf-isotope analysis with an excimer laser, depth profiling, ablation of complex geometries, and concomitant age estimation. *Chemical Geology* **209**, 121–135.

Yakymchuk, C. & Brown, M. (2014). Consequences of open-system melting in tectonics. *Journal of the Geological Society* **171**, 21–40.

Yakymchuk, C., Siddoway, C.S., Fanning, C.M., McFadden, R., Korhonen F.J. & Brown, M. (2013*a*). Anatectic reworking and differentiation of continental crust along the active margin of Gondwana: a zircon Hf–O perspective from West Antarctica. *Geological Society, London, Special Publications*, **383**, 169–210.

Yakymchuk, C., Brown, M., Ivanic, T.J. & Korhonen F.J. (2013*b*). Leucosome distribution in migmatitic paragneisses and orthogneisses: a record of self-organized melt migration and entrapment in a heterogeneous partially molten crust. *Tectonophysics*, **603**, 136–154.

Yakymchuk, C., Brown, M., Clark, C., Korhonen, F. J., Piccoli, P. M., Siddoway, C. S., Taylor, R. J. M., Vervoort, J. D. (2015). Decoding polyphase migmatites using geochronology and phase equilibria modelling. *Journal of Metamorphic Geology* **33**, 203–230.

Yakymchuk, C., Brown, M., Brown, C., Siddoway, C.S., & Fanning, C.M. 2015b. Paleozoic evolution of western Marie Byrd Land, Antarctica. *Geological Society of America Bulletin.*doi: 10.1130/B1136.1

Zeng, L., Asimow, P.D. & Saleeby, J.B. (2005a). Coupling of anatectic reactions and dissolution of accessory phases and the Sr and Nd isotope systematics of anatectic melts from a metasedimentary source. *Geochimica et Cosmochimica Acta*, **69**, 3671–3682.

Zeng, L., Saleeby, J. B. & Asimow, P. (2005b). Nd isotope disequilibrium during crustal anatexis: A record from the Goat Ranch migmatite complex, southern Sierra Nevada batholith, California. *Geology,* **33**, 53–56.

Zeng, L., Saleeby, J. B. & Ducea, M. (2005c). Geoche mical characteristics of crustal anatexis during the formation of migmatite at the Southern Sierra Nevada, California. *Contributions to Mineralogy and Petrology*, **150**, 386–402.

FIGURE CAPTIONS

Fig. 1. Geometrical reconstruction of the East Gondwana active convergent margin (modified from Figure 4 of Veevers, (2012))

Fig. 2. (a) Geological map and (b, c) schematic cross-sections (no vertical exaggeration) of the Fosdick migmatite–granite complex (modified from Siddoway *et al.*, 2004a; McFadden *et al.*, 2010b; Yakymchuk *et al.*, 2013a). (d) Sample location map of the Fosdick complex.

Fig. 3. (a) Stromatic leucosomes in migmatitic paragneiss. (b) Peritectic garnet and cordierite in leucosomes in migmatitic paragneiss. (c) Anastomosing network of leucosomes in migmatitic orthogneiss. (d) Peritectic garnet surrounded by leucosome in migmatitic orthogneiss.

Fig. 4. (a) Sheeted leucogranite complex in the Eastern Fosdick Mountains. Sub-horizontal m- to decametre-scale leucogranite sheets contain schollen of paragneiss, orthogneiss and mafic rocks. Cliff height is approximately 600 m. (b) Residual paragneiss unit with multiple discordant leucogranite bodies that intersect to form a pipe in the centre of the photograph. Red circle indicates a person for scale. (c) Concordant and discordant granite bodies in migmatite paragneiss. The red circle contains a person for scale and indicates the sampling location of Y1-AE051. (d) Heterogeneous garnet-bearing granite that contains schollen of paragneiss and mafic rocks (sample Y1-IG062). The cliff height is approximately 100m. (e) Discordant granite intruding migmatite paragneiss (sample 10CY-41). Field notebook for scale. (f) K-feldspar rich granite (sample 10CY-039).

Fig. 5. Cumulate microstructures in Cretaceous granites from the Fosdick migmatite–granite complex. (a, b) Coarse plagioclase grains with interstitial quartz and K-feldspar. (c, d) Euhedral plagioclase grains in contact with interstitial quartz. (e, f) Interlocking plagioclase and K-feldspar crystals with interstitial quartz. (g, h) Heterogeneous K-feldspar granite with coarse-grained phenocrysts of K-feldspar. (i, j) Granite comprising K-feldspar and plagioclase grains with interstitial quartz.

Fig. 6. Cathodoluminescence images of representative zircon grains from orthogneisses and

Cretaceous granites. Cathodoluminescence images were collected on different dates and so exhibit some variation in quality or sharpness. The contrast of images of individual zircons was adjusted to best display internal zoning.

Fig. 7. U–Pb Tera–Wasserberg (1972) concordia plots of LA-ICP-MS zircon data for orthogneisses and granites. Data point error ellipses and age uncertainties are reported at 2σ confidence.

Fig. 8. U–Pb Tera–Wasserberg (1972) concordia plots of SHRIMP zircon data for orthogneisses and granites from the Fosdick Complex. Error ellipses and age uncertainties are reported at 2σ confidence.

Fig. 9. Major oxide data for Swanson Formation (n = 9), Ford Granodiorite suite (n = 25), and Fosdick Complex paragneisses, orthogneisses and Cretaceous granites. The shaded fields for the Ford Granodiorite suite are based on the data from this study and data from Korhonen *et al.* (2010b), Weaver *et al.* (1991, 1992), Pankhurst *et al.* (1998), and Tulloch *et al.* (2009*a*). FeO* represents total ferrous iron. Aluminum saturation index (ASI) = molar [Al_2O_3 / CaO + Na_2O + K_2O]. Oxides are plotted as weight percent.

Fig. 10. Trace element data for Swanson Formation (n=9), Ford Granodiorite suite (n = 25), and Fosdick Complex paragneisses, orthogneisses and Cretaceous granites. The fields for the Ford Granodiorite suite are based on the data from this study and data from Korhonen *et al.* (2010b),

Weaver *et al.* (1991, 1992), Pankhurst *et al.* (1998), and Tulloch *et al.* (2009*a*). Trace element abundances are plotted as parts per million (ppm).

Fig. 11. Chondrite-normalized rare earth element (REE) patterns for paragneiss, orthogneiss and their putative protoliths. Data are from this study and Korhonen *et al.* (2010b). Chondrite normalization values from McDonough & Sun (1995)

Fig. 12. Chondrite-normalized rare earth element (REE) patterns for Cretaceous granites from the Fosdick complex (data from this study and Korhonen *et al.*, 2010b). Chondrite normalization after McDonough & Sun (1995)

Fig. 13. Sr–Nd isotopic compositions at 100 Ma for potential source rocks and granites from the Ford Ranges. Data are from this study and Korhonen *et al.* (2010b), Weaver *et al.* (1992) and Weaver *et al.* (1991). Tick marks along mixing curve are at 10% increments. The uncertainty on each data point is smaller than the symbols.

Fig. 14. (a) Variation of $\delta^{18}O$ and εHf_t in zircon *versus* $^{238}U/^{206}Pb$ age for migmatitic orthogneisses. (b) $\delta^{18}O$ *versus* εHf_{360} for migmatitic orthogneiss. The range of εHf values for the Swanson Formation represents the interquartile range of zircon values recalculated to 360 Ma and the $\delta^{18}O$ value range is from oxygen isotope analysis of six whole-rock samples (Yakymchuk *et al.*, 2015b). The εHf and $\delta^{18}O$ values of the Ford Granodiorite are from Yakymchuk *et al.* (2013a, 2015b). The $\delta^{18}O$ value of mantle-derived rocks is 5·3 ± 0·6‰

(Valley *et al.*, 1998). The cross in the bottom left shows the approximate ±2σ uncertainties for individual Hf and O isotope values.

Fig. 15. (a) Variation of $\delta^{18}O$ and εHf_t in zircon *versus* $^{238}U/^{206}Pb$ age for Cretaceous granites from the Fosdick complex. (b) $\delta^{18}O$ *versus* εHf_{100} for granites from the Fosdick Complex. Also shown are the ranges of zircon εHf and $\delta^{18}O$ values for three potential sources: Swanson Formation, Ford Granodiorite suite and the mantle. For the Swanson Formation, a portion of the interquartile range of εHf values of detrital zircon recalculated to 100 Ma is shown (the interquartile range extends from -13·9 to -30·3). The $\delta^{18}O$ value range of the Swanson Formation is based on oxygen isotope analysis of six whole-rock samples (Yakymchuk *et al.*, 2015b). The εHf and $\delta^{18}O$ values of the Ford Granodiorite suite are from Yakymchuk *et al.* (2013a, 2015b). The $\delta^{18}O$ value of mantle-derived rocks is 5·3 ± 0·6‰ (Valley *et al.*, 1998). Two binary mixing models were calculated for mixing between anatectic melt from the Ford Granodiorite suite (FGD) with anatectic melt from the Swanson Formation or the assimilation of the Swanson Formation *en masse* using representative end-members (stars) of each source as discussed in the text. The cross in the bottom left shows the approximate ±2σ uncertainties for individual Hf and O isotope values. The dashed field represents the range of εHf values of Devonian–Carboniferous zircon from Y1-IG062 recalculated to 100 Ma.

Fig. 16. Calculated *P–T* pseudosections for a representative composition of: (a) Swanson Formation, (b) Ford Granodiorite suite, (c) migmatitic paragneiss and (d) migmatitic orthogneiss. The thick dashed line represents the solidus and the thin dashed lines represent melt isopleths in mol.% (~vol.%). The fields outlined by the thick black lines represent the range of peak *P–T*

conditions estimated for the Devonian–Carboniferous metamorphism (Yakymchuk *et al.*, 2015) in (a) and (b), and the range of *P–T* conditions estimated for the final solidus assemblage during the Cretaceous event in (c) and (d). The red lines in (c) and (d) represent the assumed thermal gradient (770°C/GPa) for thickened crust in Marie Byrd Land prior to crustal thinning associated with the exhumation of the Fosdick Complex and an average thermal gradient though the *P–T* conditions estimated for the final solidus assemblage after decompression (1230°C/GPa) from Yakymchuk *et al.* (2013a).

Fig. 17. Ternary (Na+Ca)–(Fe*+Mg+Ti)–K plot (after Solar & Brown, 2001) comparing the compositions of granites from this study with experimental glass compositions (Skjerlie *et al*., 1993; Patiño Douce & Harris, 1998; Koester *et al.*, 2002). See text for details.

Fig. 18. Log - log trace element plots for Rb, Sr, Ba and Rb/Sr showing fractionation trends for K-feldspar, plagioclase and biotite compared with the Cretaceous granites from the Fosdick migmatite–granite Complex. The amount of fractional crystallization is shown by 10% increments. Distribution coefficients for Rb, Sr, and Ba in K-feldspar and plagioclase are the average of values reported for each mineral in Nash & Crecraft (1985).

Fig. 19. Compilation of geochronological data for rocks from the Fosdick migmatite–granite Complex. Data sources as follows: [a]Korhonen *et al.* (2012), [b]Yakymchuk *et al.* (2015a), [c]Richard *et al.* (1994), [d]Saito *et al.* (2013), [e]Yakymchuk *et al.* (2013*a*), [f]Korhonen *et al.* (2010*b*), [g]McFadden *et al.* (2010*a*), [h]McFadden *et al.* (2010*b*).

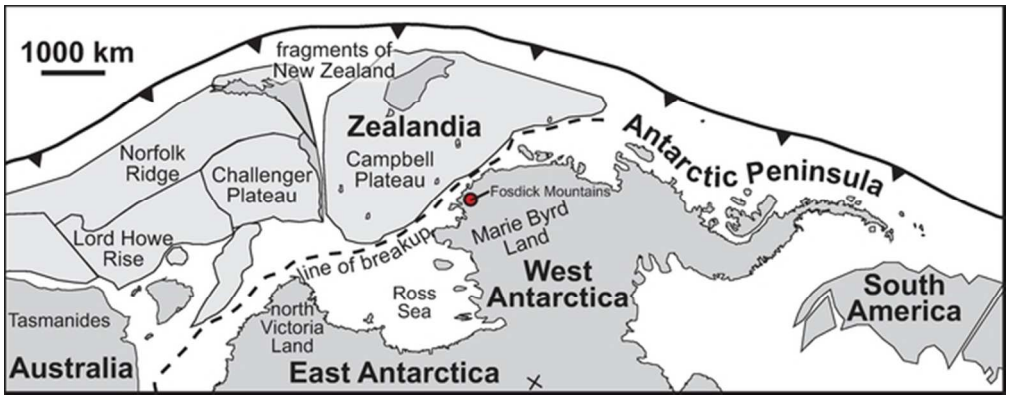

Figure 1
57x22mm (300 x 300 DPI)

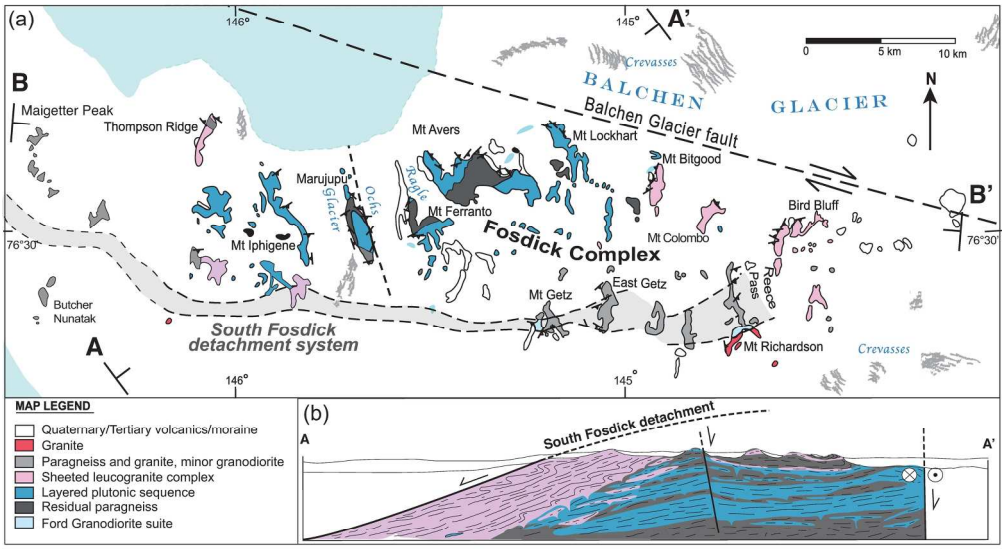

Figure 2 (1 of 2)
209x148mm (300 x 300 DPI)

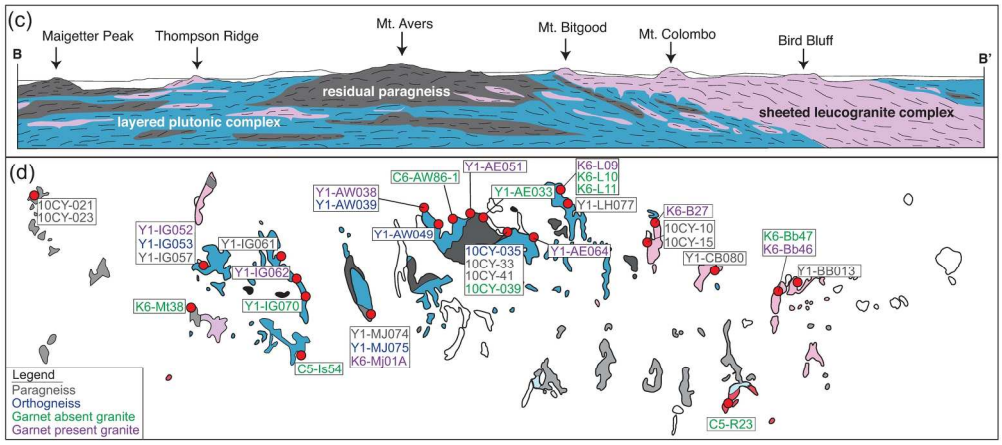

Figure 2 (2 of 2)
209x148mm (300 x 300 DPI)

Figure 3
165x193mm (300 x 300 DPI)

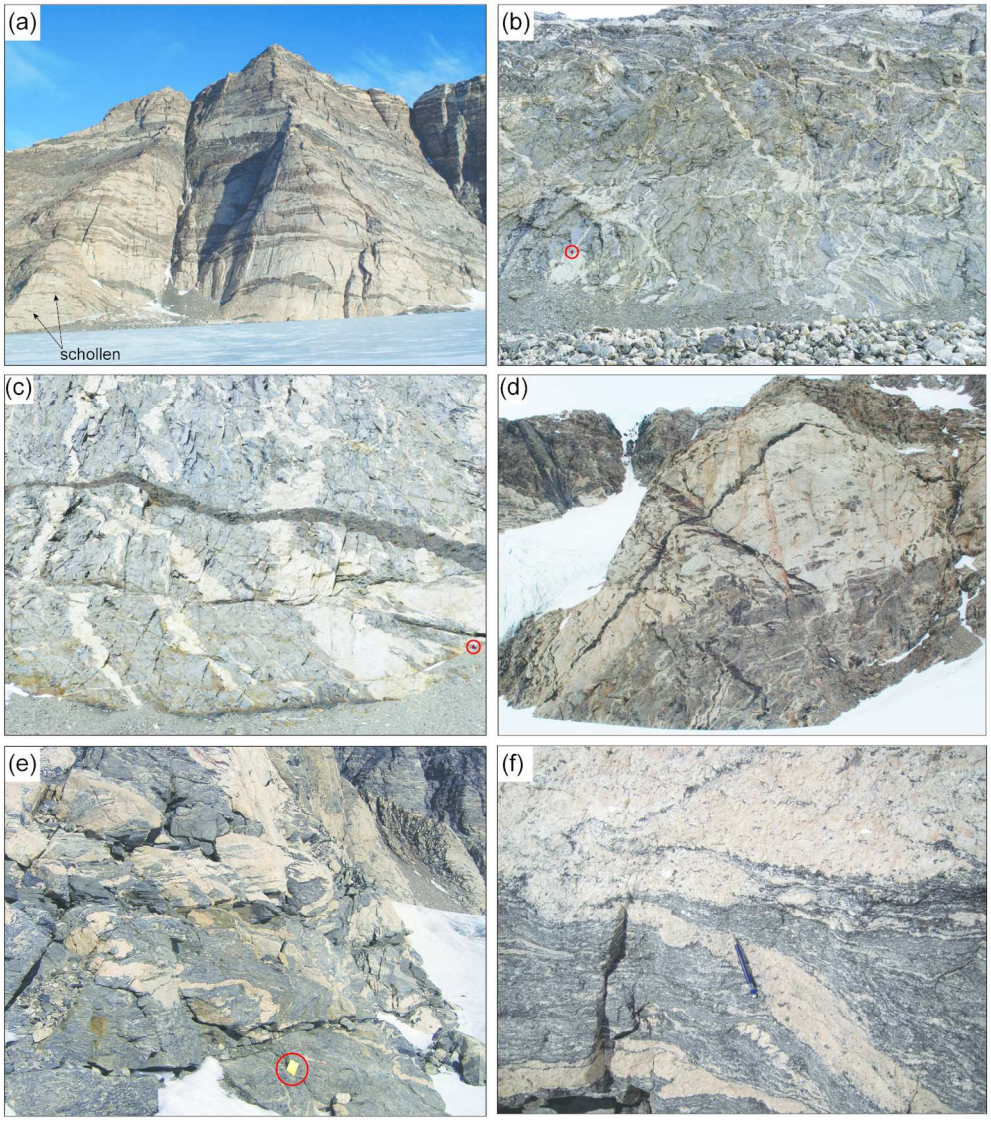

Figure 4
143x160mm (300 x 300 DPI)

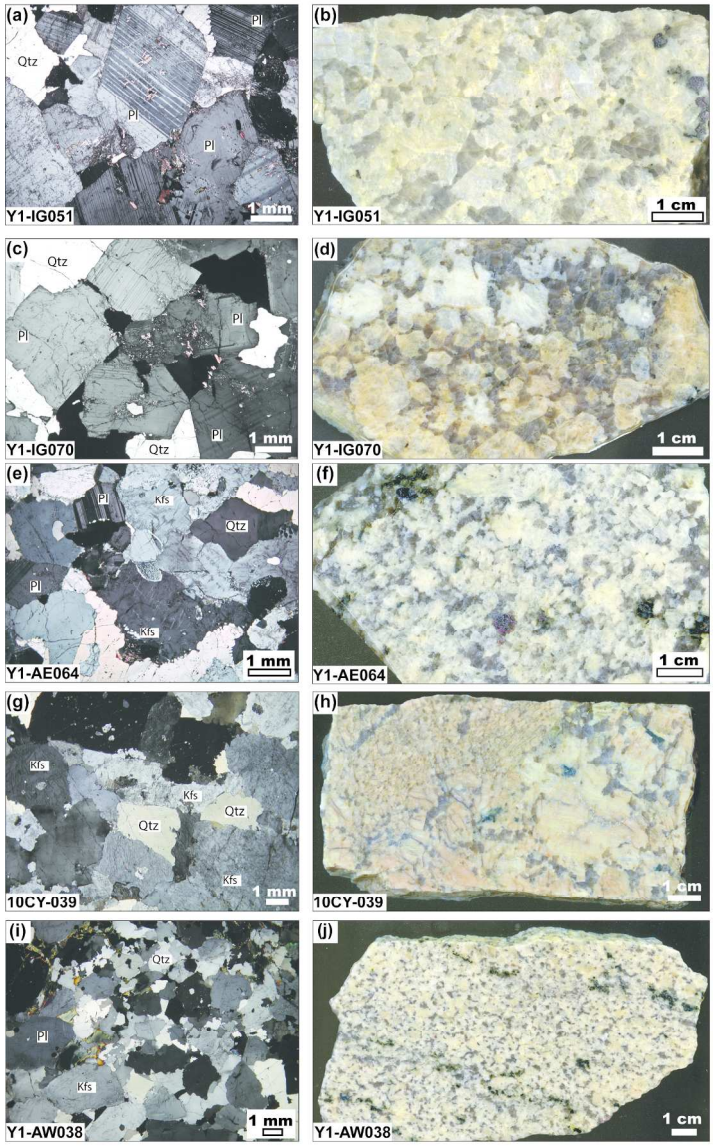

Figure 5
158x249mm (300 x 300 DPI)

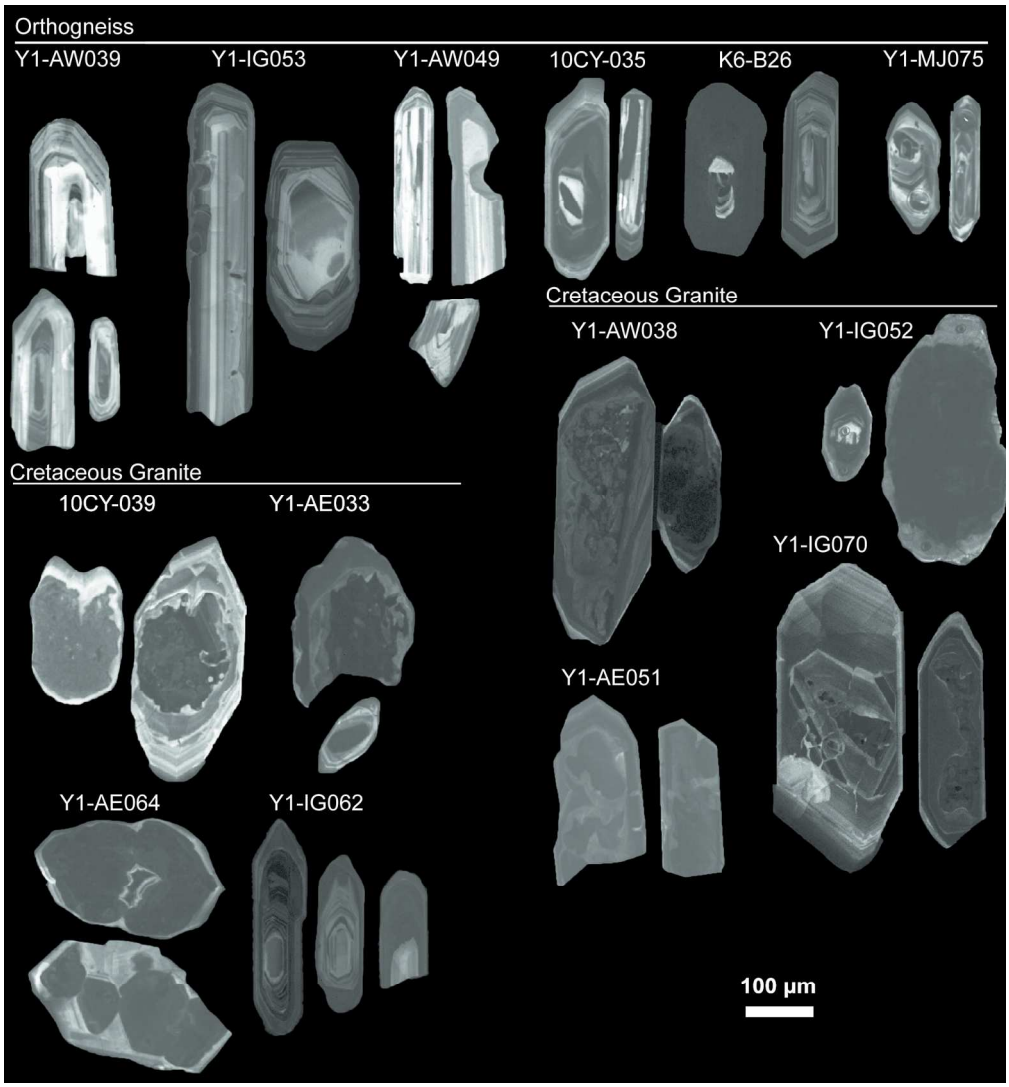

Figure 6
159x171mm (300 x 300 DPI)

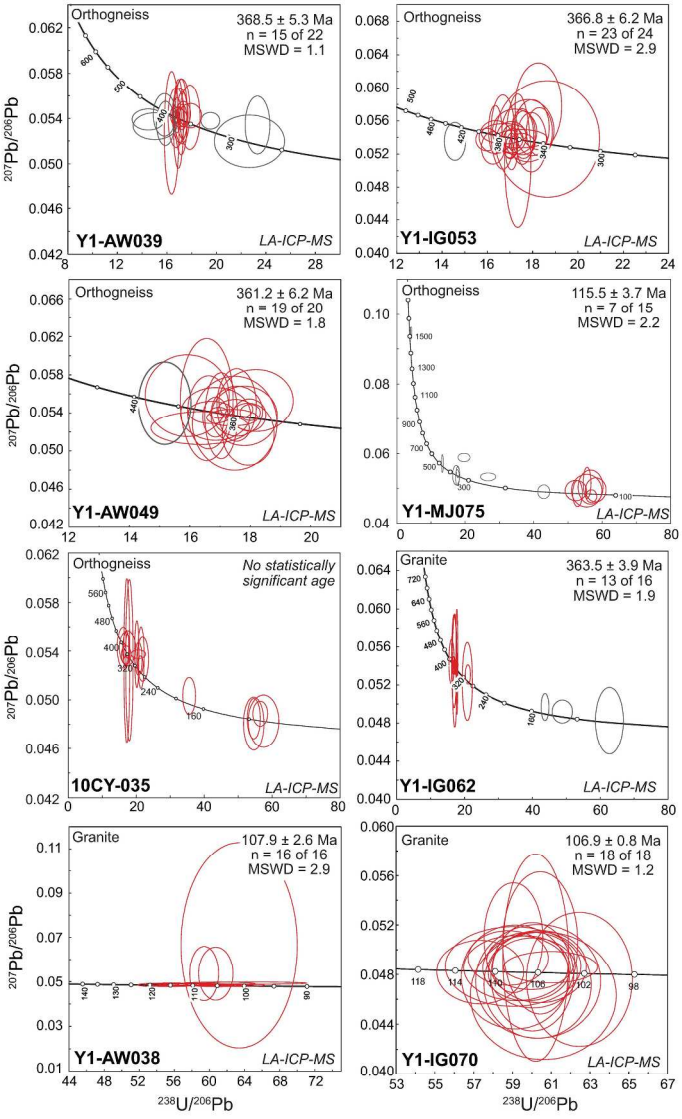

Figure 7 (1 of 2)
279x361mm (300 x 300 DPI)

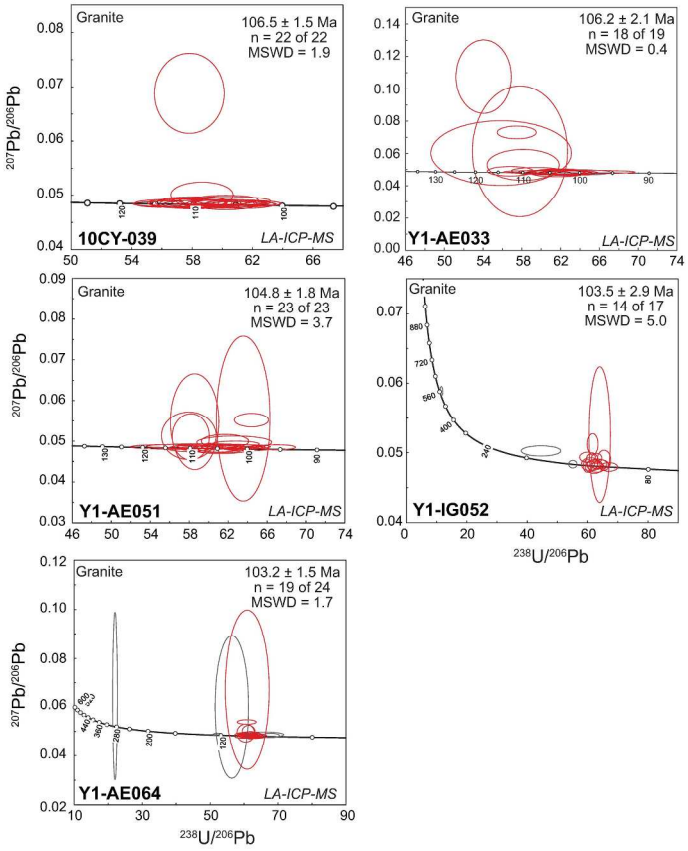

Figure 7 (2 of 2)
279x361mm (300 x 300 DPI)

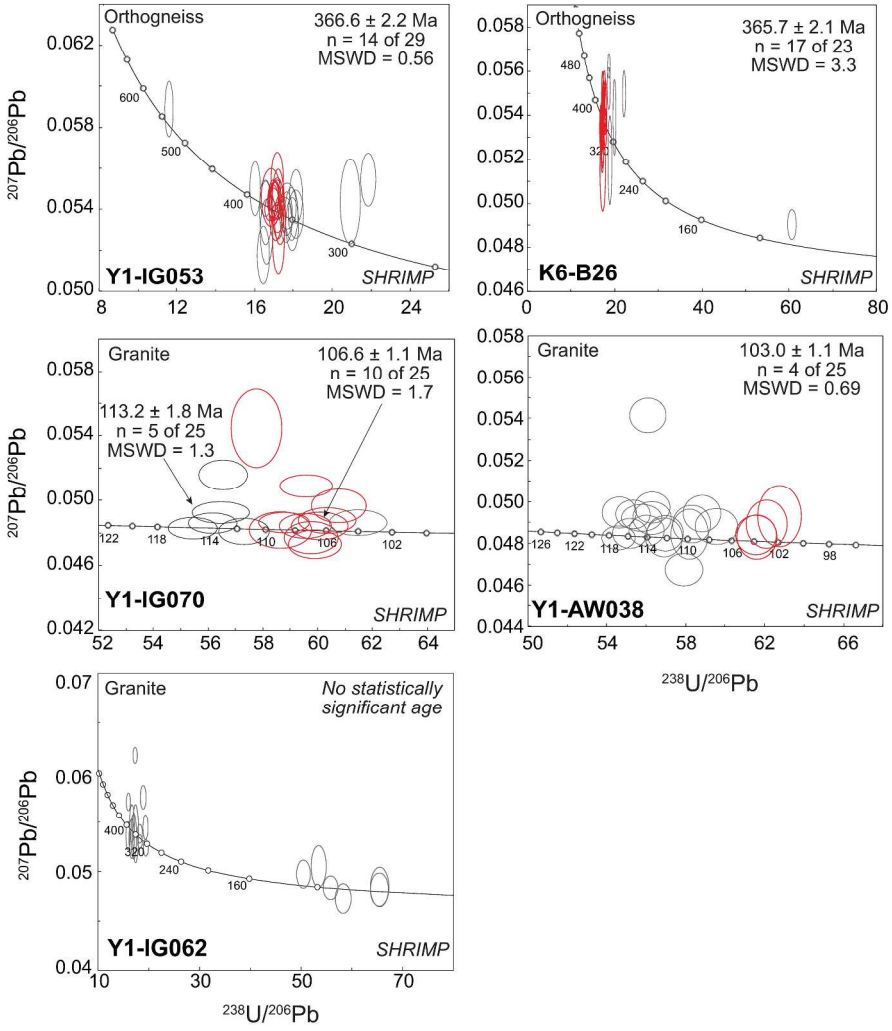

Figure 8
279x361mm (300 x 300 DPI)

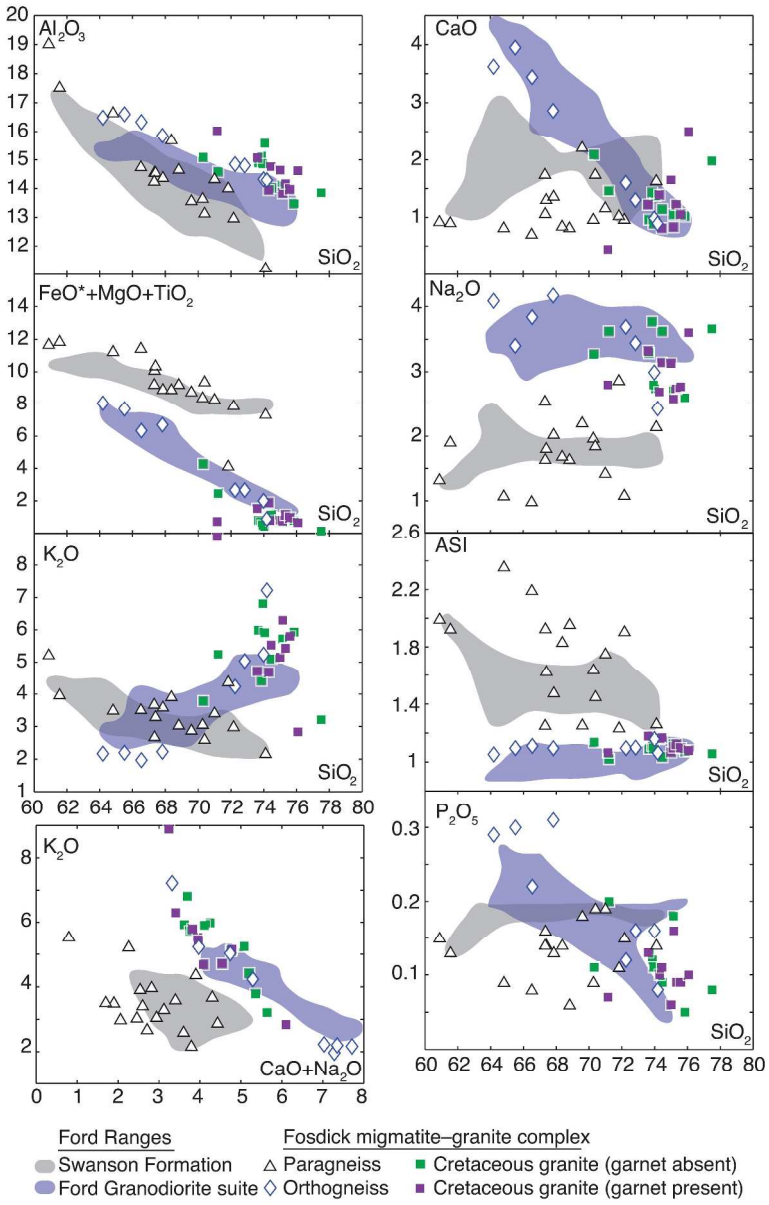

Figure 9
270x428mm (300 x 300 DPI)

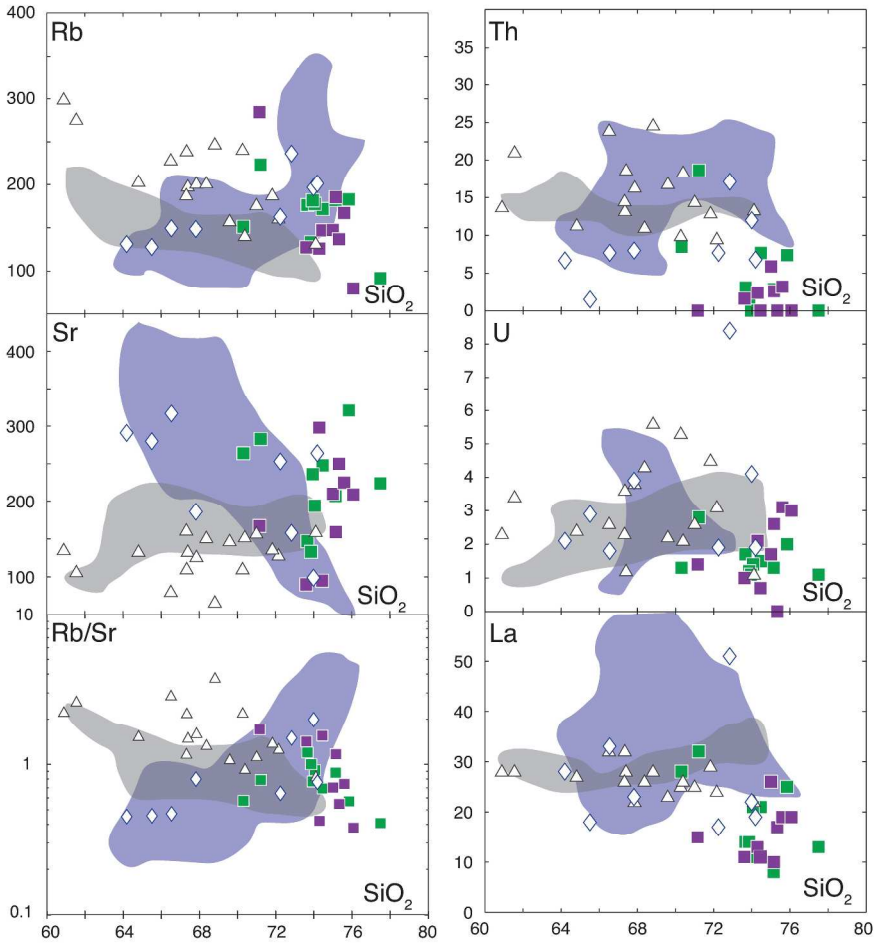

Figure 10 (1 of 2)
279x361mm (300 x 300 DPI)

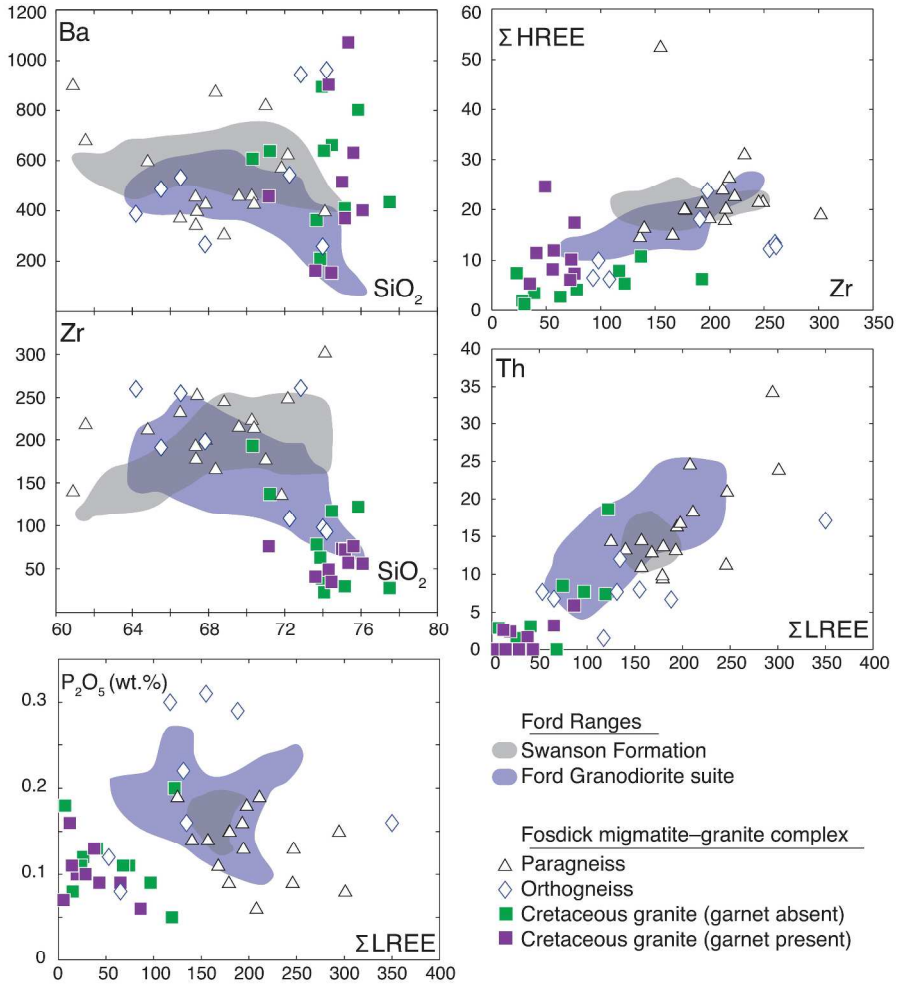

Figure 10 (2 of 2)
279x361mm (300 x 300 DPI)

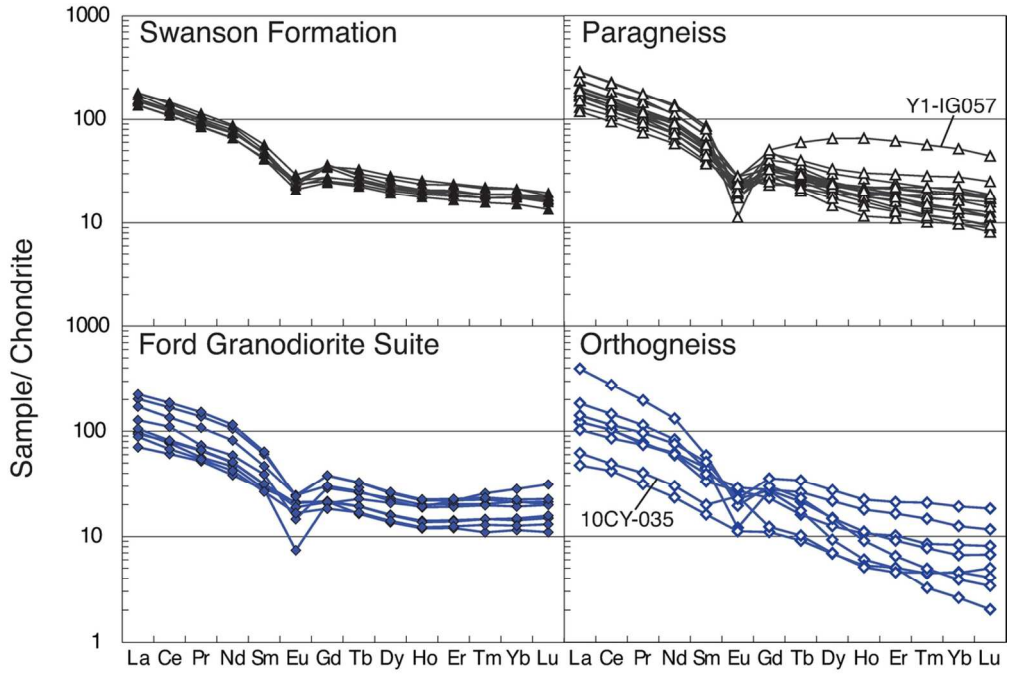

Figure 11
110x74mm (300 x 300 DPI)

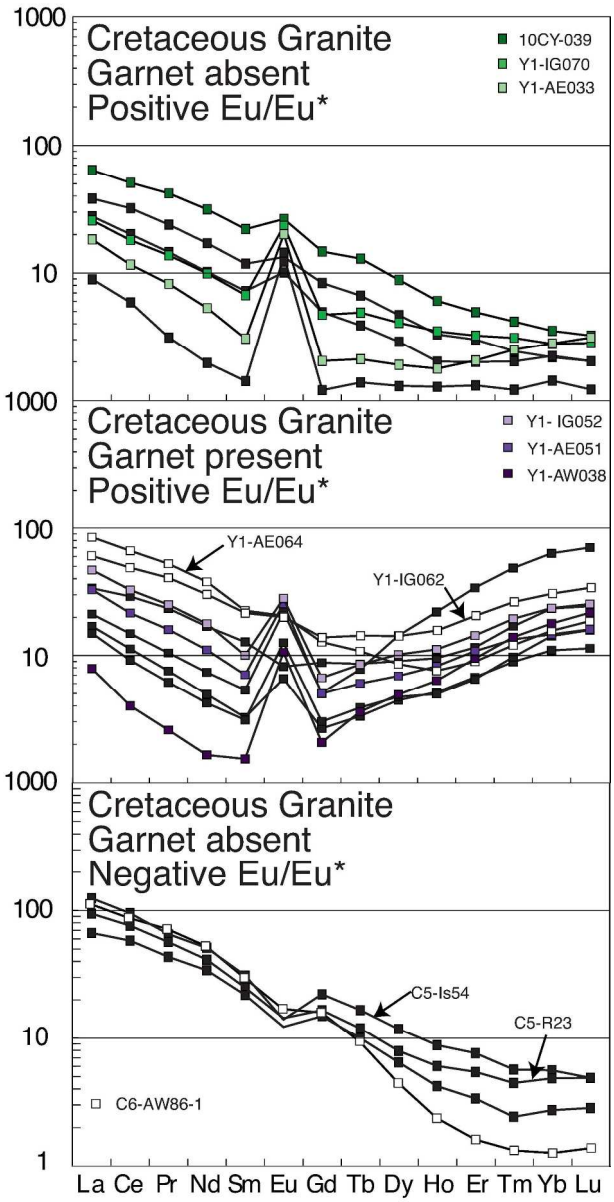

Figure 12
162x321mm (300 x 300 DPI)

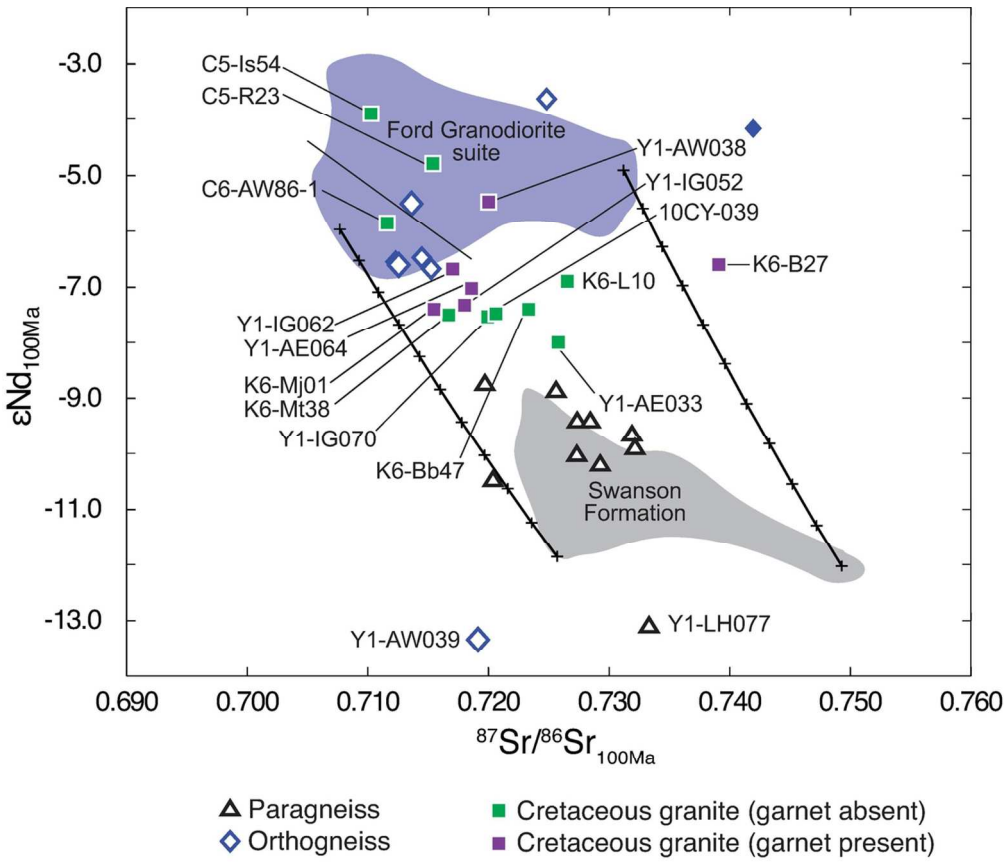

Figure 13
114x98mm (300 x 300 DPI)

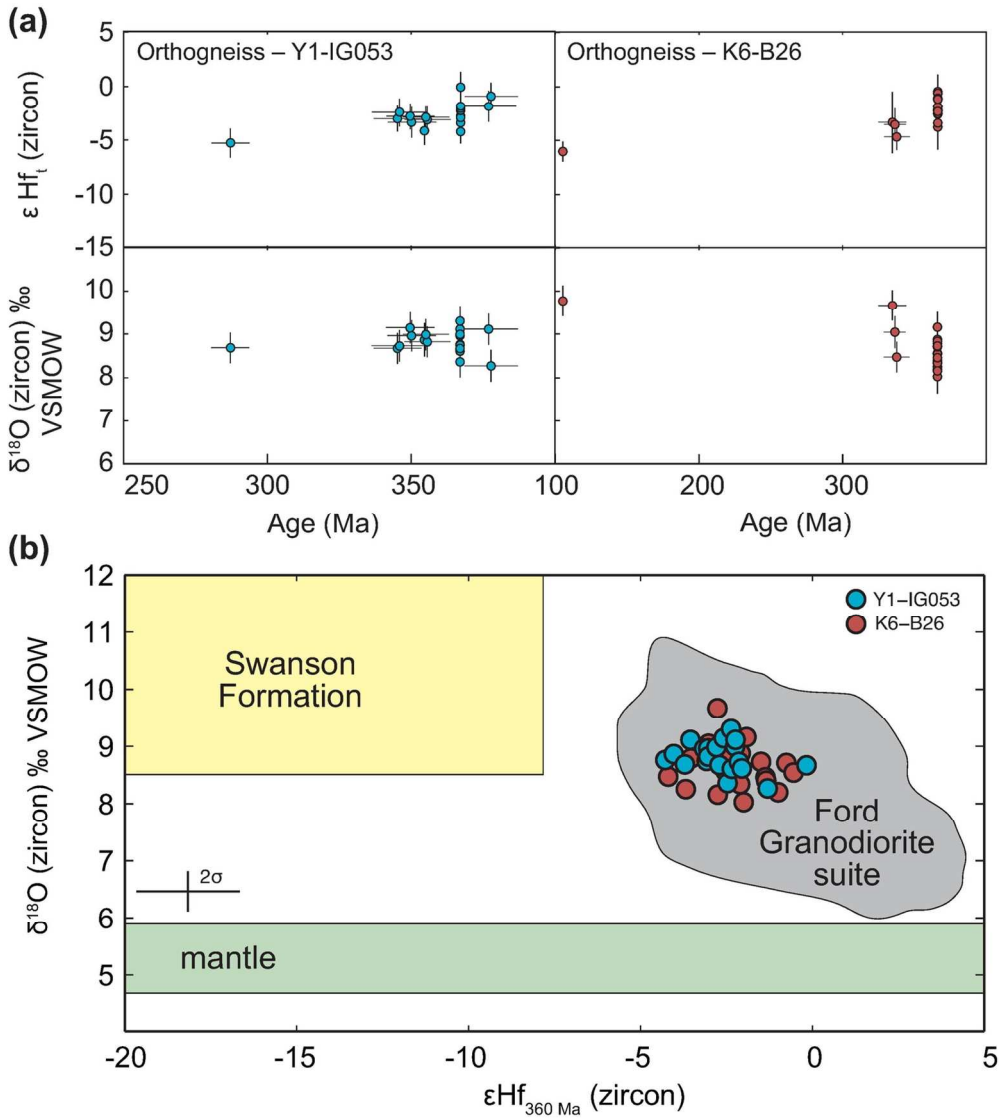

Figure 14
131x147mm (300 x 300 DPI)

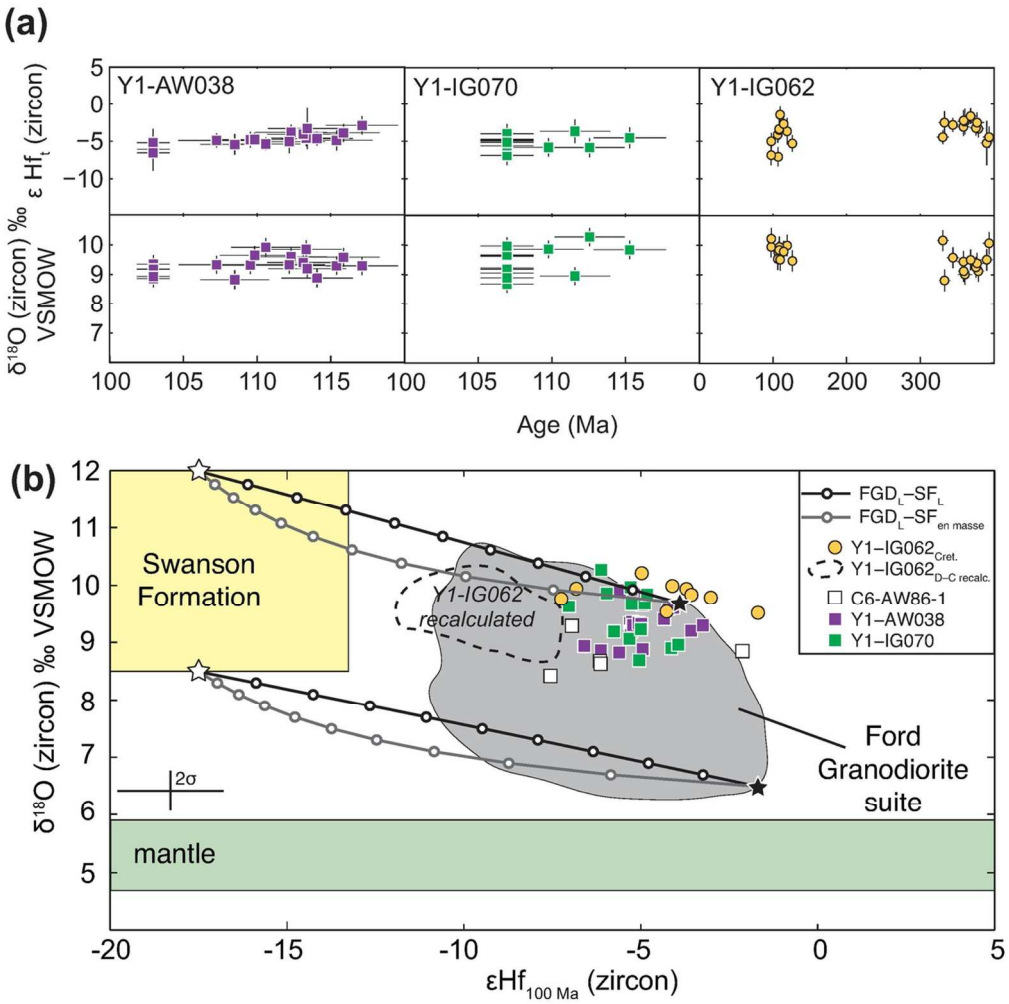

Figure 15
115x115mm (300 x 300 DPI)

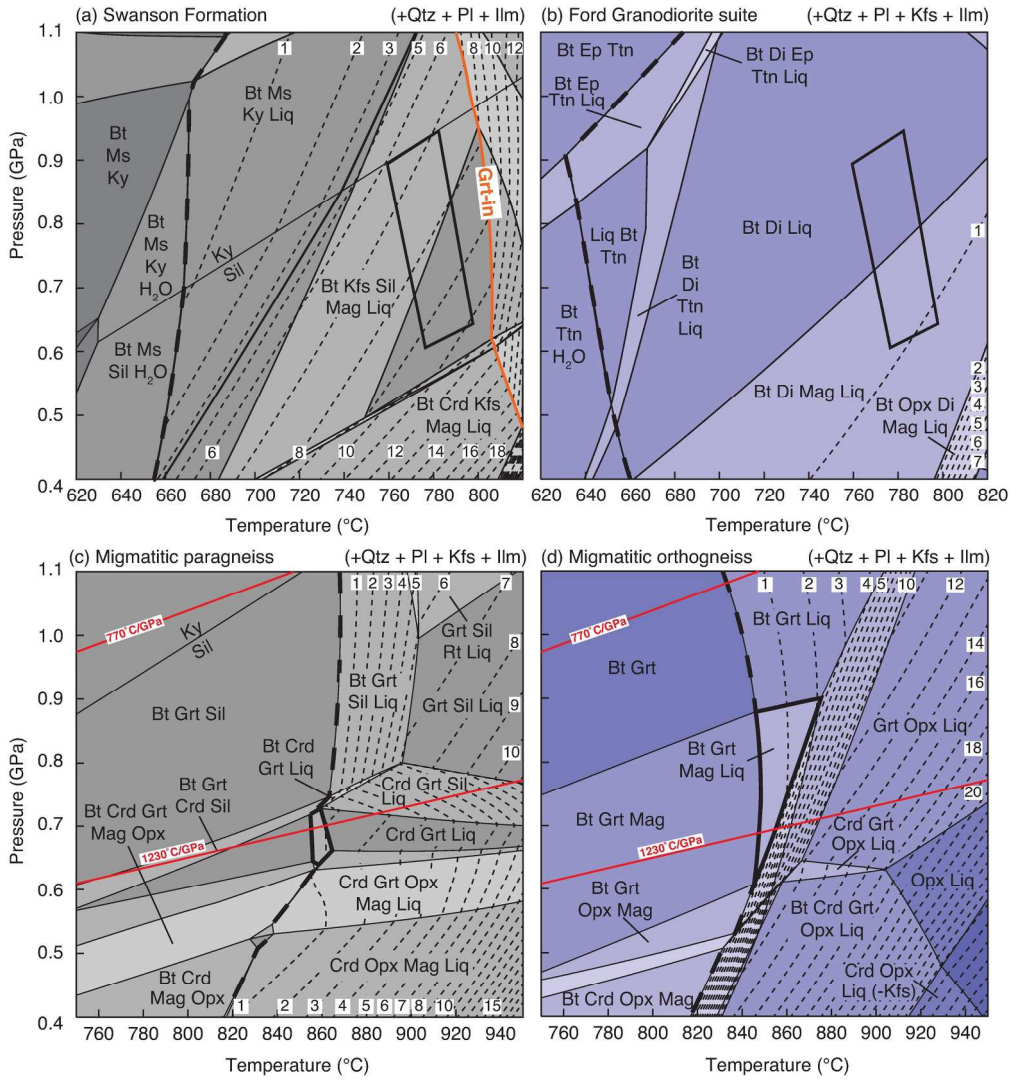

Figure 16
205x220mm (300 x 300 DPI)

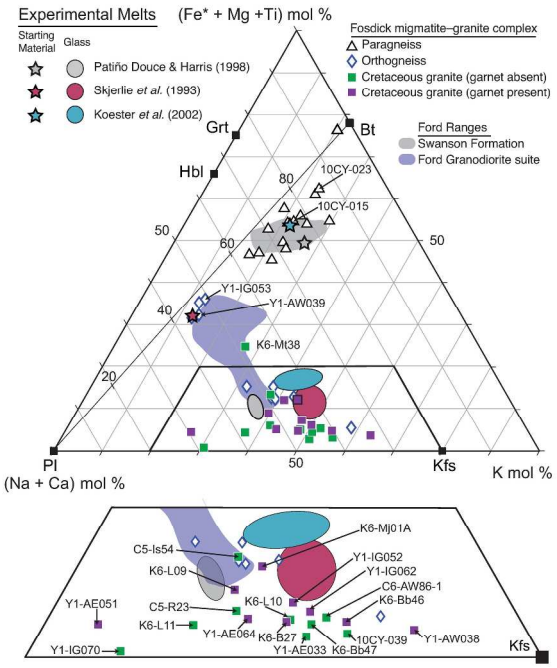

Figure 17
279x361mm (300 x 300 DPI)

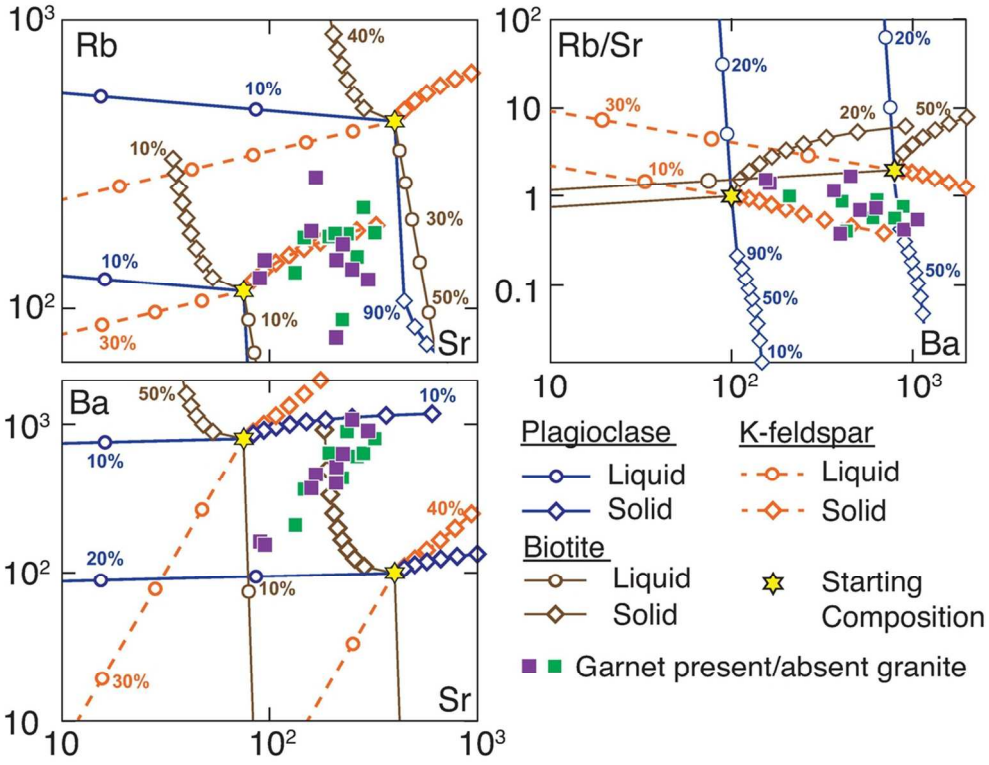

Figure 18
102x80mm (300 x 300 DPI)

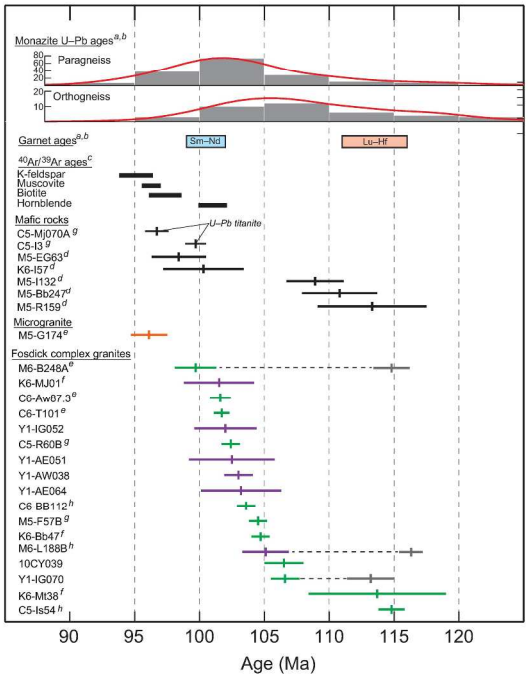

Figure 19
279x361mm (300 x 300 DPI)

Table 1. Summary of U–Pb geochronology results

Sample	Method	U–Pb age	MSWD	n
Orthogneiss				
Y1-AW039	LA-ICP-MS	368.5 ± 5.3	1.1	15
Y1-IG053	LA-ICP-MS	366.8 ± 6.2	2.9	23 of 24
	SHRIMP	366.6 ± 2.2	0.56	14 of 17
K6-B26	SHRIMP	365.7 ± 2.1	3.3	17
Y1-AW049	LA-ICP-MS	361.2 ± 6.2	1.8	19 of 20
Y1-MJ075	LA-ICP-MS	115.5 ± 3.7	2.2	7
10CY-035	LA-ICP-MS	c. 360, 320, 100	–	–
Granites				
Y1-IG062	LA-ICP-MS	363.5 ± 3.9	1.9	13 of 16
	SHRIMP	*No Age*	–	–
Y1-AW038	LA-ICP-MS	107.9 ± 2.6	2.9	16
	SHRIMP	103.0 ± 1.1	0.69	4 of 25
Y1-IG070	LA-ICP-MS	106.9 ± 0.8	1.2	18
	SHRIMP	106.6 ± 1.1	1.7	10 of 25
10CY-039	LA-ICP-MS	106.5 ± 1.5	1.9	22
Y1-AE033	LA-ICP-MS	106.2 ± 2.1	0.4	18 of 19
Y1-AE051	LA-ICP-MS	104.8 ± 1.8	3.7	23
Y1-IG052	LA-ICP-MS	103.5 ± 2.9	4	14 of 17
Y1-AE064	LA-ICP-MS	103.2 ± 1.5	1.7	19 of 24

Table 2: Major element, trace element and REE concentrations

Rock Type:	Paragneiss							
Sample:	10CY-010	10CY-015	10CY-021	10CY-023	10CY-033	10CY-041	Y1-BB013	Y1-CB080
wt %								
SiO_2	61·55	68·82	67·40	66·51	67·85	67·32	60·89	70·39
TiO_2	0·94	0·81	0·94	1·05	0·76	0·77	0·85	0·76
Al_2O_3	17·54	14·67	14·56	14·76	14·39	14·26	19·04	13·15
Fe_2O_3	1·32	1·24	0·76	1·06	1·36	1·08	1·21	0·67
FeO	6·05	4·55	5·50	5·87	4·21	4·61	5·87	5·04
MnO	0·09	0·05	0·07	0·08	0·08	0·05	0·07	0·08
MgO	3·71	2·76	3·26	3·59	2·74	2·89	3·90	3·00
CaO	0·91	0·82	1·31	0·71	1·37	1·75	0·93	1·75
Na_2O	1·91	1·64	1·81	0·99	2·03	2·55	1·33	1·85
K_2O	3·98	3·05	3·31	3·52	3·60	3·69	5·23	2·61
P_2O_5	0·13	0·06	0·14	0·08	0·13	0·14	0·15	0·19
LOI	2·21	1·77	1·50	1·90	1·85	1·18	2·65	1·69
Total	100·34	100·24	100·56	100·12	100·37	100·29	100·12	100·05
ppm (XRF)								
Rb	276	247	198	228	201	188	299	141
Sr	106	66	133	80	126	161	135	152
Y	40	29	34	37	33	33	35	29
Zr	218	245	253	232	200	193	140	214
V	138	113	127	135	110	110	121	115
Ni	76	50	51	61	51	51	54	53
Cr	188	139	141	159	141	129	120	118
Nb	22	32	19	28	22	15	22	17
Ga	26	28	22	27	23	20	29	20
Cu	43	15	13	5	18	10	11	14
Zn	138	141	114	138	107	110	129	100
Co	28	21	22	27	20	20	23	22
Ba	682	306	399	373	428	456	901	427
La	28	28	28	32	22	26	28	26
Ce	74	57	65	75	54	54	72	68
U	3 ·4	5·6	1·2	2·6	3·8	2·3	2·3	2·1
Th	21	25	19	24	16	15	14	18
Sc	18	15	17	13	16	14	16	15
Pb	<1	<1	<1	<1	<1	<1	18	14
ppm (ICP-MS)								
Sc	18·4	13·8	–	16·7	13·6	14·2	16·6	13·4
Y	40·5	34·4	–	45·2	28·0	34·4	23·9	25·9
La	57·1	47·8	–	68·7	43·9	35·6	41·5	48·6
Ce	114	97·0	–	140	91·1	72·7	83·7	98·4
Pr	13·5	11·3	–	16·5	10·7	8·72	9·58	11·5
Nd	51·6	43·1	–	63·2	40·6	33·1	37·5	44·0
Sm	10·3	8·72	–	12·8	7·96	6·89	7·61	8·56
Eu	1·60	0·98	–	1·09	1·13	1·22	1·41	1·31
Gd	8·07	6·66	–	9·31	5·79	5·65	5·75	6·35
Tb	1·33	1·11	–	1·45	0·94	0·99	0·90	0·98
Dy	7·36	6·11	–	8·19	5·21	5·90	4·76	5·19
Ho	1·47	1·17	–	1·66	0·99	1·23	0·87	0·93
Er	3·90	3·07	–	4·70	2·56	3·43	2·12	2·24
Tm	0·55	0·43	–	0·70	0·36	0·50	0·27	0·29
Yb	3·31	2·64	–	4·47	2·17	3·14	1·56	1·73
Lu	0·43	0·35	–	0·62	0·28	0·43	0·20	0·23

(continued)

Table 2: Continued

Rock Type:	Paragneiss				Orthogneiss			
Sample:	Y1-IG057	Y1-IG061	Y1-LH077	Y1-MJ074	10CY-035	Y1-AW039	Y1-AW049	Y1-IG053
wt %								
SiO_2	42·01	71·00	69·59	68·37	74·19	67·82	64·19	65·51
TiO_2	1·57	0·68	0·76	0·74	0·08	0·76	0·92	0·89
Al_2O_3	23·10	14·34	13·58	15·71	14·29	15·85	16·48	16·60
Fe_2O_3	3·89	0·94	1·06	1·00	0·06	0·91	1·65	1·03
FeO	12·78	4·34	4·17	4·53	0·50	3·42	3·70	3·86
MnO	0·44	0·09	0·04	0·09	0·01	0·08	0·07	0·07
MgO	7·74	2·45	2·90	2·75	0·23	1·71	1·95	2·02
CaO	0·43	1·17	2·22	0·85	0·89	2·86	3·62	3·95
Na_2O	0·37	1·43	2·21	1·69	2·43	4·17	4·09	3·40
K_2O	5·54	3·42	2·89	3·92	7·22	2·23	2·17	2·20
P_2O_5	0·15	0·19	0·18	0·14	0·08	0·31	0·29	0·30
LOI	3·49	2·22	1·42	2·30	0·43	1·18	1·08	1·01
Total	99·44	100·53	100·06	100·29	100·04	100·50	99·54	100·26
ppm (XRF)								
Rb	394	176	158	201	201	149	131	128
Sr	18	157	147	151	264	186	291	280
Y	91	38	32	31	5·9	31	16	25
Zr	155	177	215	166	93	198	260	191
V	222	95	103	105	15	93	101	102
Ni	90	55	49	55	4	14	12	12
Cr	166	98	128	107	24	59	61	65
Nb	39	13	15	17	3	20	17	14
Ga	39	19	19	22	15	24	23	23
Cu	69	16	5	7	3	10	5	17
Zn	296	81	102	100	14	74	88	78
Co	51	18	18	19	<1	14	17	16
Ba	262	822	459	875	963	267	388	486
La	16	25	23	26	19	23	28	18
Ce	53	60	59	63	32	49	60	38
U	1·2	2·6	2·2	4·3	1·9	3·9	2·1	2·9
Th	34	14	17	11	6·8	8·0	6·7	1·5
Sc	41	11	14	14	<1	14	16	16
Pb	<1	14	20	22	47	2	14	15
ppm (ICP-MS)								
Sc	58·17	12·59	12·49	10·88	1·46	13·92	14·80	14·76
Y	99·2	34·3	31·5	21·8	7·83	33·7	15·7	26·0
La	68·0	28·1	45·1	35·9	14·7	33·4	43·5	24·5
Ce	138	57·9	91·9	72·7	30·1	70·3	89·2	52·5
Pr	16·2	6·87	10·8	8·57	3·74	8·94	10·6	6·89
Nd	60·7	26·6	41·6	33·2	13·8	34·8	38·3	27·7
Sm	12·0	5·54	8·38	6·66	2·95	7·56	6·55	5·82
Eu	0·63	1·53	1·58	1·34	1·35	1·28	1·28	1·63
Gd	10·1	4·62	6·54	4·97	2·45	7·09	5·44	5·52
Tb	2·16	0·84	1·06	0·78	0·37	1·23	0·77	0·95
Dy	16·0	5·41	5·84	4·21	1·71	6·76	3·67	5·33
Ho	3·58	1·20	1·11	0·79	0·28	1·22	0·61	0·98
Er	9·84	3·55	2·82	2·04	0·73	3·38	1·46	2·63
Tm	1·40	0·54	0·37	0·29	0·11	0·52	0·19	0·36
Yb	8·36	3·48	2·18	1·74	0·73	3·10	1·07	2·01
Lu	1·09	0·46	0·28	0·23	0·12	0·45	0·17	0·29

(continued)

Table 2: Continued

Rock Type:	Orthogneiss	Cretaceous granite						
Sample:	Y1-MJ075	10CY-039	Y1-IG062	C6-AW86-1	Y1-AE051	Y1-AE064	Y1-IG052	Y1-IG070
wt %								
SiO_2	72·84	73·95	75·60	75·85	76·08	75·01	75·33	77·50
TiO_2	0·29	0·04	0·01	0·08	0·02	0·04	0·02	0·01
Al_2O_3	14·80	14·85	13·97	13·47	14·62	14·64	14·17	13·85
Fe_2O_3	0·28	0·08	0·03	0·05	0·11	0·22	0·11	0·03
FeO	1·49	0·22	0·76	0·43	0·39	0·40	0·83	0·08
MnO	0·03	0·01	0·06	0·01	0·03	0·05	0·07	0·01
MgO	0·63	0·15	0·17	0·22	0·14	0·18	0·20	0·00
CaO	1·30	0·89	1·05	1·02	2·50	1·65	1·22	1·98
Na_2O	3·44	2·80	2·77	2·60	3·60	3·13	2·74	3·66
K_2O	5·03	6·81	5·80	5·93	2·84	5·15	5·43	3·21
P_2O_5	0·16	0·11	0·09	0·05	0·10	0·06	0·09	0·08
LOI	0·69	0·61	0·58	0·39	0·65	0·48	0·48	0·33
Total	100·46	99·93	100·39	99·76	100·47	100·57	100·30	100·42
ppm (XRF)								
Rb	236	182	167	183	80	147	137	91·6
Sr	158	236	225	321	209	210	250	224
Y	13	4·8	27·4	3	14·7	10·3	15·5	4
Zr	261	39	76	122	56	73	57	28
V	26	5	<1	12	1	6	6	1
Ni	6	6	2	2	2	3	2	1
Cr	28	35	21	11	33	21	18	19
Nb	17·2	2	1·2	2	1	2·1	0·9	0·8
Ga	20·8	14·9	14·2	15	17·4	15·9	14·1	15·8
Cu	4	4	7	3	2	4	7	25
Zn	41	11	11	13	9	13	10	7
Co	1	<1	<1	<1	<1	<1	<1	<1
Ba	945	895	632	803	402	515	1073	434
La	51	11	19	25	19	26	17	13
Ce	122	13	37	53	23	39	20	17
U	8·4	1·1	3·1	2	3	1·7	<0·5	1·1
Th	17·1	<0·5	3·2	7·4	<0·5	5·9	<0·5	<0·5
Sc	5	<1	4	<1	4	2	3	1
Pb	38	65	52	36	46	47	62	43
ppm (ICP-MS)								
Sc	5·03	0·79	7·32	1·11	4·51	3·96	6·40	0·51
Y	14·4	5·63	24·9	3·50	12·7	11·9	17·8	2·95
La	93·4	6·12	14·4	27·6	7·79	20·1	11·1	4·34
Ce	169	11·1	30·0	55·4	13·2	40·7	20·1	7·14
Pr	18·3	1·28	3·79	6·87	1·48	4·86	2·32	0·76
Nd	60·3	4·54	13·8	24·9	5·06	17·3	8·13	2·43
Sm	8·73	0·99	3·20	4·54	1·04	3·33	1·48	0·45
Eu	1·10	1·32	1·13	0·98	1·44	1·16	1·58	1·13
Gd	5·97	0·94	2·77	3·25	0·99	2·54	1·33	0·41
Tb	0·83	0·18	0·52	0·34	0·22	0·39	0·31	0·08
Dy	3·61	1·00	3·51	1·12	1·70	2·10	2·51	0·47
Ho	0·50	0·19	0·86	0·13	0·45	0·41	0·61	0·10
Er	1·04	0·52	3·31	0·26	1·73	1·43	2·30	0·33
Tm	0·12	0·08	0·65	0·03	0·33	0·30	0·48	0·06
Yb	0·63	0·45	4·95	0·21	2·36	2·51	3·80	0·45
Lu	0·08	0·07	0·84	0·03	0·39	0·46	0·62	0·08

(continued)

Table 2: Continued

Rock Type:	Cretaceous granite		Microgranite	Other Granite			
Sample:	Y1-AW038	Y1-AE033	10CY-024	21220-3	Billey Bluff	Y2-MP083	Y2-BR087
wt %							
SiO_2	71·16	74·06	74·25	74·96	75·53	75·44	74·63
TiO_2	0·03	0·10	0·28	0·14	0·21	0·21	0·16
Al_2O_3	16·02	15·58	13·99	13·26	13·28	12·59	13·51
Fe_2O_3	0·04	0·09	0·12	0·17	0·55	0·60	0·15
FeO	0·54	0·14	1·31	0·55	0·58	1·16	1·20
MnO	0·08	0·01	0·03	0·01	0·05	0·04	0·04
MgO	0·11	0·10	0·31	0·34	0·23	0·20	0·19
CaO	0·44	1·37	1·20	1·10	0·63	0·86	1·14
Na_2O	2·80	2·74	2·82	2·29	4·28	3·55	3·23
K_2O	8·89	5·91	5·34	6·31	4·58	4·55	4·93
P_2O_5	0·07	0·11	0·07	0·15	0·05	0·05	0·07
LOI	0·47	0·62	0·78	0·40	0·43	0·63	0·70
Total	100·24	100·23	99·87	99·34	100·03	99·38	99·38
ppm (XRF)							
Rb	284	178	195	239	228	358	267
Sr	167	194	222	191	119	86	121
Y	14·6	8·9	33·7	6·6	23·1	27·4	35·7
Zr	76	23	227	130	189	126	145
V	5	8	23	17	17	18	19
Ni	1	1	1	1	1	1	2
Cr	14	8	4	26	15	31	65
Nb	2·4	2·2	14·8	7·2	32·6	32·9	27·7
Ga	14·9	18·5	20	17·3	24·1	24·8	23·3
Cu	4	3	7	1	4	1	2
Zn	13	10	27	24	31	41	45
Co	<1	<1	2	<1	<1	<1	1
Ba	457	640	834	427	461	252	557
La	15	21	48	25	56	39	37
Ce	13	28	108	52	109	72	80
U	1·4	1·4	2·4	2·6	5·3	5·8	3·7
Th	<0·5	<0·5	35·7	13	34·6	33·6	13·5
Sc	3	1	3	3	2	7	8
Pb	64	58	29	48	12	26	17
ppm (ICP-MS)							
Sc	3·57	1·04	3·80	–	–	–	–
Y	10·9	9·77	35·4	–	–	–	–
La	1·87	15·2	66·2	45·3	59·8	39·7	74·9
Ce	2·45	31·3	141	56·4	79·2	44·4	92·2
Pr	0·24	3·90	17·1	9·46	10·2	7·63	16·1
Nd	0·75	14·4	62·7	33·0	32·4	26·1	55·0
Sm	0·23	3·26	11·0	5·67	4·65	4·85	9·05
Eu	0·6	1·49	1·22	0·79	0·55	0·43	0·74
Gd	0·41	2·93	8·33	3·96	3·41	4·10	6·59
Tb	0·13	0·47	1·25	0·48	0·51	0·70	0·92
Dy	1·21	2·17	6·65	2·00	3·04	4·27	4·91
Ho	0·35	0·33	1·26	0·26	0·59	0·81	0·84
Er	1·51	0·79	3·68	0·52	1·81	2·43	2·31
Tm	0·34	0·10	0·56	0·06	0·32	0·42	0·38
Yb	2·87	0·57	3·38	0·32	2·13	2·77	2·56
Lu	0·53	0·08	0·52	0·05	0·35	0·43	0·40

Table 3: Sr–Nd isotope compositions

Rock Type	Paragneiss							Orthogneiss		
Sample no·	10CY-010	10CY-015	10CY-023	10CY-033	Y1-CB080	Y1-IG057	Y1-LH077	10CY-035	Y1-AW039	Y1-IG053
Rb (ppm)	284·9	246·8	232·4	206·5	147·3	453·1	164·7	196·2	131·3	114·4
Sr (ppm)	104·4	64·28	99·59	98·35	144·3	11·92	139·3	269·8	181·0	285·9
Rb/Sr	2·729	3·840	2·333	2·100	1·021	38·02	1·182	0.7272	0·7253	0·4002
$^{87}Rb/^{86}Sr$	7·919	11·1	6·762	6·090	2·960	111·8	3·429	2·105	2·101	1·159
$^{87}Sr/^{86}Sr$	0·739606	0·747548	0·729249	0·734213	0·731586	0·876719	0·738234	0·718274	0·721603	0·716186
$^{87}Sr/^{86}Sr_{(100Ma)}$	0·728538	0·731965	0·719797	0·725700	0·727449	0·720467	0·733440	0·715331	0·718667	0·714567
$^{87}Sr/^{86}Sr_{(360Ma)}$	0·699687	0·691346	0·695159	0·703511	0·716666	0·313191	0·720946	0·707661	0·711013	0·710346
Sm (ppm)	13·23	9·802	10·50	7·233	7·593	12·45	7·506	2·494	6·301	6·469
Nd (ppm)	69·90	51·43	46·59	35·57	38·56	65·74	38·24	11·52	28·76	34·52
Sm/Nd	0·1893	0·1906	0·2253	0·2034	0·1969	0·1895	0·1963	0·2166	0·2191	0·1874
$^{147}Sm/^{144}Nd$	0·1144	0·1152	0·1210	0·1229	0·1190	0·1145	0·1187	0·1309	0·1324	0·1133
$^{143}Nd/^{144}Nd$	0·512100	0·512089	0·512139	0·512134	0·512073	0·512046	0·511914	0·512255	0·511908	0·512254
$\varepsilon Nd_{(0Ma)}$	-10·5	-10·7	-9·7	-9·8	-11·0	-11·5	-14·1	-7·4	-14.2	-7·5
$\varepsilon Nd_{(100Ma)}$	-9·4	-9·6	-8·7	-8·9	-10·0	-10·5	-13·1	-6·6	-13·4	-6·4
$\varepsilon Nd_{(360Ma)}$	-6·7	-6·9	-6·2	-6·4	-7·4	-7·7	-10·5	-4·4	-11·3	-3·6

Rock Type	Orthogneiss		Cretaceous Granite							
Sample no·	Y1-AW049	Y1-MJ075	10CY-039	Y1-IG062	C6-AW86-1	Y1-AE064	Y1-IG052	Y1-IG070	Y1-AW038	Y1-AE033
Rb (ppm)	133·2	224·8	164·9	154·4	167·2	130·7	131·0	84·6	255·2	154·9
Sr (ppm)	288·3	156·5	240·1	225·8	328·8	210·7	252·9	219·1	172·3	195·2
Rb/Sr	0·4620	1·436	0·6871	0·6838	0·5085	0·6204	0·5180	0·3860	1·481	0·7934
$^{87}Rb/^{86}Sr$	1·337	4·164	1·901	1·987	1·472	1·736	1·532	1·118	4·244	2·125
$^{87}Sr/^{86}Sr$	0·714254	0·730827	0·723275	0·719905	0·713751	0·721116	0·719866	0·721597	0·726049	0·728855
$^{87}Sr/^{86}Sr_{(100Ma)}$	0·712385	0·725007	0·720617	0·717127	0·711694	0·718689	0·717725	0·720034	0·720117	0·725884
$^{87}Sr/^{86}Sr_{(360Ma)}$	0·707513	0·709837	0·713690	0·709887	0·706332	0·712365	0·712143	0·715961	0·704654	0·718141
Sm (ppm)	6·532	6·997	0·4368	3·471	4·972	2·625	1·073	0·4497	0·3425	2·927
Nd (ppm)	38·37	46·79	1·975	15·02	25·77	13·39	5·652	2·956	1·120	12·29
Sm/Nd	0·1702	0·1496	0·2211	0·2310	0·1930	0·1961	0·1898	0·1521	0·3057	0·2382
$^{147}Sm/^{144}Nd$	0·1029	0·0904	0·1337	0·1361	0·1166	0·1133	0·1400	0·0919	0·1848	0·1440
$^{143}Nd/^{144}Nd$	0·512238	0·512380	0·512211	0·512259	0·512284	0·512221	0·512208	0·512183	0·512348	0·512192
$\varepsilon Nd_{(0Ma)}$	-7·8	-5·0	-8·3	-7·4	-6·9	-8·1	-8·4	-8·8	-5·6	-8·7
$\varepsilon Nd_{(100Ma)}$	-6·6	-3·6	-7·5	-6·6	-5·8	-7·1	-7·3	-7·5	-5·5	-8·0
$\varepsilon Nd_{(360Ma)}$	-3·5	-0·1	-5·4	-4·7	-3·2	-4·5	-4·6	-4·1	-5·1	-6·2

Notes:

$\lambda_{Rb} = 1{\cdot}3968 \times 10^{-11}$

$\lambda_{Sm} = 6{\cdot}54 \times 10^{-12}$

$^{143}Nd/^{144}Nd_{CHUR\ (0)} = 0{\cdot}512638$

$^{147}Sm/^{144}Nd_{CHUR(0)} = 0{\cdot}1967$

Table 4: Zircon Hf and O isotope analyses

spot	assigned age (Ma)	$^{18}O/^{16}O$	$\pm10^{-7}$	$\delta^{18}O$ ‰	± 2 S·E·	$^{176}Hf/^{177}Hf$	$\pm10^{-6}$	$^{176}Lu/^{177}Hf$	$\pm10^{-5}$	$\varepsilon_{Hf(0)}$	$^{176}Hf/^{177}Hf_{(t)}$	$\varepsilon_{Hf(t)}$	± 2 S·E·	$\varepsilon_{Hf(360)}$	$\varepsilon_{Hf(100)}$
Y1-IG053 – orthogneiss															
IG053-1·1	345	0·0020439	1	8·67	0·35	0·282485	34	0·00050	1	-10·6	0·282482	-3·0	1·2	-2·7	–
IG053-1·2	377	0·0020448	2	9·11	0·36	0·282503	41	0·00121	7	-10·0	0·282495	-1·9	1·5	-2·2	–
IG053-2·1	350	0·0020449	1	9·14	0·36	0·282488	34	0·00045	1	-10·5	0·282486	-2·8	1·2	-2·6	–
IG053-2·2	533	0·0020400	1	6·75	0·35	0·282328	41	0·00116	12	-16·1	0·282317	-4·7	1·5	-8·4	–
IG053-3·2	367	0·0020441	2	8·74	0·36	0·282480	40	0·00131	5	-10·8	0·282471	-2·9	1·4	-3·1	–
IG053-4·2	367	0·0020448	1	9·11	0·35	0·282465	40	0·00110	2	-11·3	0·282458	-3·4	1·4	-3·6	–
IG053-5·1	367	0·0020439	1	8·67	0·35	0·282560	40	0·00101	4	-7·9	0·282554	0·0	1·4	-0·2	–
IG053-5·2	287	0·0020439	1	8·68	0·35	0·282460	38	0·00101	3	-11·5	0·282455	-5·3	1·3	–	–
IG053-6·1	356	0·0020442	1	8·82	0·35	0·282475	35	0·00041	1	-10·9	0·282473	-3·1	1·2	-3·0	–
IG053-6·2	367	0·0020433	1	8·36	0·35	0·282492	32	0·00055	5	-10·3	0·282489	-2·3	1·1	-2·5	–
IG053-7·1	367	0·0020438	2	8·61	0·37	0·282497	35	0·00077	1	-10·2	0·282492	-2·2	1·2	-2·4	–
IG053-8·1	367	0·0020441	2	8·76	0·36	0·282441	31	0·00059	2	-12·1	0·282437	-4·1	1·1	-4·3	–
IG053-9·1	346	0·0020440	2	8·73	0·36	0·282503	37	0·00079	3	-10·0	0·282498	-2·4	1·3	-2·1	–
IG053-13·1	367	0·0020438	2	8·61	0·36	0·282509	38	0·00136	3	-9·7	0·282500	-1·9	1·3	-2·1	–
IG053-14·1	350	0·0020445	2	8·96	0·36	0·282476	40	0·00104	3	-10·9	0·282470	-3·4	1·4	-3·2	–
IG053-16·1	367	0·0020445	1	8·96	0·35	0·282477	35	0·00070	1	-10·9	0·282473	-2·9	1·2	-3·0	–
IG053-17·1	367	0·0020452	1	9·30	0·35	0·282501	30	0·00146	4	-10·0	0·282491	-2·2	1·1	-2·4	–
IG053-18·1	355	0·0020443	3	8·87	0·38	0·282447	37	0·00045	1	-11·9	0·282444	-4·2	1·3	-4·1	–
IG053-18·2	367	0·0020446	0	8·99	0·35	0·282497	41	0·00037	1	-10·2	0·282495	-2·1	1·5	-2·3	–
IG053-19·1	355	0·0020445	1	8·98	0·35	0·282484	28	0·00072	1	-10·6	0·282480	-2·9	1·0	-2·8	–
IG053-19·2	378	0·0020431	2	8·27	0·37	0·282526	35	0·00071	2	-9·1	0·282521	-0·9	1·2	-1·3	–

(continued)

Table 4: Continued

spot	assigned age (Ma)	$^{18}O/^{16}O$	$\pm10^{-7}$	$\delta^{18}O$ ‰	± 2 S·E·	$^{176}Hf/^{177}Hf$	$\pm10^{-6}$	$^{176}Lu/^{177}Hf$	$\pm10^{-5}$	$\varepsilon_{Hf(0)}$	$^{176}Hf/^{177}Hf_{(t)}$	$\varepsilon_{Hf(t)}$	± 2 S·E·	$\varepsilon_{Hf(360)}$	$\varepsilon_{Hf(100)}$
K6-B26 – Orthogneiss															
K6B26-1·1	366	0·0020437	3	8·56	0·37	0·282494	42	0·00110	2	-10·0	0·282487	-2·4	1·5	-2·5	–
K6B26-2·1	338	0·0020435	0	8·47	0·35	0·282448	34	0·00125	4	-11·9	0·282441	-4·7	1·2	-4·2	–
K6B26-3·1	336	0·0020447	2	9·04	0·36	0·282479	42	0·00093	3	-10·2	0·282474	-3·5	1·5	-3·0	–
K6B26-4·2	366	0·0020429	5	8·20	0·42	0·282536	48	0·00090	3	-10·6	0·282530	-0·9	1·7	-1·0	–
K6B26-6·1	366	0·0020429	2	8·16	0·36	0·282485	36	0·00073	3	-9·1	0·282481	-2·6	1·3	-2·8	–
K6B26-7·1	366	0·0020432	1	8·34	0·35	0·282505	34	0·00095	7	-9·5	0·282499	-2·0	1·2	-2·1	–
K6B26-8·1	366	0·0020435	1	8·46	0·35	0·282527	40	0·00113	3	-9·1	0·282520	-1·2	1·4	-1·4	–
K6B26-9·1	366	0·0020443	1	8·88	0·35	0·282510	38	0·00164	6	-8·8	0·282499	-2·0	1·3	-2·1	–
K6B26-10·1	366	0·0020433	2	8·37	0·36	0·282505	36	0·00127	5	-8·5	0·282497	-2·0	1·3	-2·2	–
K6B26-10·2	366	0·0020426	3	8·03	0·39	0·282509	52	0·00113	14	-8·2	0·282502	-1·9	1·8	-2·0	–
K6B26-11·1	366	0·0020430	1	8·25	0·35	0·282475	59	0·00312	5	-7·9	0·282454	-3·6	2·1	-3·7	–
K6B26-12·1	366	0·0020433	2	8·40	0·36	0·282526	46	0·00089	3	-7·6	0·282520	-1·2	1·6	-1·4	–
K6B26-13·1	366	0·0020441	2	8·79	0·36	0·282464	38	0·00088	2	-7·3	0·282458	-3·4	1·3	-3·6	–
K6B26-14·1	366	0·0020442	1	8·84	0·35	0·282490	41	0·00075	3	-7·0	0·282485	-2·5	1·5	-2·6	–
K6B26-15·2	366	0·0020436	1	8·54	0·36	0·282549	45	0·00096	0	-6·7	0·282543	-0·4	1·6	-0·6	–
K6B26-16·1	335	0·0020459	1	9·67	0·35	0·282486	81	0·00091	4	-6·4	0·282481	-3·3	2·9	-2·8	–
K6B26-17·1	366	0·0020440	2	8·71	0·36	0·282542	43	0·00080	5	-6·1	0·282537	-0·6	1·5	-0·8	–
K6B26-18·1	366	0·0020440	1	8·73	0·35	0·282521	33	0·00076	4	-5·7	0·282516	-1·4	1·2	-1·5	–
K6B26-19·1	366	0·0020449	1	9·16	0·35	0·282511	47	0·00108	1	-5·4	0·282504	-1·8	1·7	-1·9	–
K6B26-20·1	105	0·0020461	2	9·77	0·36	0·282549	26	0·00039	0	-5·1	0·282549	-6·0	0·9	–	-6·2
Y1-IG062– granite															
IG062-1·1	98	0·0020470	2	10·21	0·36	0·282582	32	0·00047	1	-7·2	0·282582	-5·0	1·1	–	-5·0
IG062-1·2	1621	0·0020386	1	6·05	0·35	0·282082	77	0·00131	3	-24·8	0·282042	10·3	2·7	–	–
IG062-2·1	110	0·0020456	2	9·51	0·37	0·282675	31	0·00048	0	-3·9	0·282675	-1·5	1·1	–	-1·7
IG062-2·2	344	0·0020458	1	9·58	0·35	0·282492	26	0·00064	1	-10·3	0·282488	-2·8	0·9	-2·5	–
IG062-3·1	98	0·0020465	1	9·94	0·35	0·282530	38	0·00057	2	-9·0	0·282529	-6·9	1·3	–	-6·8
IG062-4·1	331	0·0020469	1	10·16	0·35	0·282457	26	0·00111	1	-11·6	0·282451	-4·5	0·9	-3·9	–

(continued)

Table 4: Continued

spot	assigned age (Ma)	$^{18}O/^{16}O$	$\pm10^{-7}$	$\delta^{18}O$ ‰	± 2 S·E·	$^{176}Hf/^{177}Hf$	$\pm10^{-6}$	$^{176}Lu/^{177}Hf$	$\pm10^{-5}$	$\varepsilon_{Hf(0)}$	$^{176}Hf/^{177}Hf_{(t)}$	$\varepsilon_{Hf(t)}$	± 2 S·E·	$\varepsilon_{Hf(360)}$	$\varepsilon_{Hf(100)}$
IG062-6·1	359	0·0020448	1	9·12	0·35	0·282504	39	0·00128	3	-9·9	0·282496	-2·2	1·4	-2·2	–
IG062-6·2	368	0·0020456	0	9·50	0·35	0·282513	29	0·00105	1	-9·6	0·282506	-1·7	1·0	-1·9	–
IG062-6·3	126	0·0020455	1	9·47	0·36	0·282557	31	0·00073	2	-8·0	0·282556	-5·3	1·1	–	-5·9
IG062-10·1	390	0·0020456	2	9·51	0·36	0·282397	83	0·00087	9	-13·7	0·282391	-5·2	2·9	-5·9	–
IG062-10·2	361	0·0020446	1	9·02	0·35	0·282497	48	0·00103	9	-10·2	0·282491	-2·4	1·7	-2·4	–
IG062-11·1	119	0·0020466	2	9·99	0·36	0·282608	50	0·00123	9	-6·2	0·282606	-3·7	1·8	–	-4·1
IG062-11·2	377	0·0020454	2	9·39	0·36	0·282483	38	0·00101	3	-10·7	0·282476	-2·5	1·3	-2·9	–
IG062-12·1	114	0·0020462	2	9·78	0·36	0·282638	28	0·00082	2	-5·2	0·282637	-2·7	1·0	–	-3·0
IG062-12·2	393	0·0020467	3	10·06	0·37	0·282413	40	0·00033	2	-13·1	0·282411	-4·5	1·4	-5·2	–
IG062-12·3	333	0·0020442	2	8·81	0·37	0·282507	42	0·00053	2	-9·8	0·282504	-2·5	1·5	-1·9	–
IG062-14·1	109	0·0020465	2	9·94	0·36	0·282618	36	0·00060	2	-5·9	0·282617	-3·5	1·3	–	-3·7
IG062-17·1	107	0·0020457	2	9·53	0·37	0·282602	30	0·00054	1	-6·5	0·282601	-4·1	1·1	–	-4·3
IG062-18·1	108	0·0020463	1	9·84	0·35	0·282622	39	0·00070	3	-5·7	0·282621	-3·4	1·4	–	-3·6
IG062-18·2	359	0·0020455	1	9·45	0·35	0·282480	34	0·00124	5	-10·8	0·282472	-3·1	1·2	-3·1	–
IG062-19·1	375	0·0020451	1	9·25	0·35	0·282462	28	0·00079	5	-11·4	0·282457	-3·2	1·0	-3·6	–
IG062-20·1	379	0·0020448	1	9·13	0·35	0·282459	33	0·00107	7	-11·5	0·282452	-3·3	1·2	-3·8	–
IG062-21·1	107	0·0020461	2	9·76	0·36	0·282518	36	0·00057	5	-9·4	0·282517	-7·1	1·3	–	-7·3
Y1-AW038 – Granite															
AW038-1·1	103	0·0020461	2	9·35	0·31	0·282575	31	0·00106	1	-10·0	0·282573	-5·2	1·1	–	-5·3
AW038-1·2	113	0·0020471	1	9·85	0·30	0·282585	29	0·00098	1	-11·9	0·282583	-4·6	1·0	–	-4·9
AW038-3·1	113	0·0020462	1	9·40	0·30	0·282601	37	0·00131	0	-10·2	0·282599	-4·1	1·3	–	-4·4
AW038-4·2	110	0·0020460	1	9·32	0·30	0·282583	30	0·00135	3	-10·6	0·282581	-4·8	1·1	–	-5·0
AW038-5·1	103	0·0020451	1	8·87	0·30	0·282551	37	0·00155	7	-9·1	0·282549	-6·1	1·3	–	-6·2
AW038-6·1	112	0·0020466	1	9·60	0·30	0·282608	29	0·00103	1	-9·5	0·282606	-3·8	1·0	–	-4·1
AW038-6·2	107	0·0020460	1	9·33	0·30	0·282580	27	0·00088	1	-9·1	0·282579	-4·9	1·0	–	-5·1
AW038-7·1	112	0·0020460	0	9·33	0·30	0·282574	43	0·00148	4	-8·8	0·282571	-5·1	1·5	–	-5·3
AW038-8·1	103	0·0020457	2	9·18	0·31	0·282573	53	0·00046	0	-8·5	0·282573	-5·2	1·9	–	-5·3
AW038-10·1	110	0·0020467	2	9·65	0·31	0·282583	24	0·00116	2	-8·2	0·282581	-4·8	0·8	–	-5·0

(continued)

Table 4: Continued

spot	assigned age (Ma)	$^{18}O/^{16}O$	$\pm10^{-7}$	$\delta^{18}O$ ‰	± 2 S·E·	$^{176}Hf/^{177}Hf$	$\pm10^{-6}$	$^{176}Lu/^{177}Hf$	$\pm10^{-5}$	$\varepsilon_{Hf(0)}$	$^{176}Hf/^{177}Hf_{(t)}$	$\varepsilon_{Hf(t)}$	± 2 S·E·	$\varepsilon_{Hf(360)}$	$\varepsilon_{Hf(100)}$
AW038-12·1	103	0·0020452	1	8·94	0·30	0·282538	68	0·00178	4	-7·9	0·282535	-6·6	2·4	–	-6·6
AW038-14·1	111	0·0020472	2	9·92	0·31	0·282565	24	0·00085	2	-7·6	0·282564	-5·4	0·8	–	-5·6
AW038-15·1	115	0·0020459	2	9·30	0·30	0·282576	38	0·00102	2	-7·3	0·282574	-4·9	1·3	–	-5·2
AW038-16·1	108	0·0020450	2	8·83	0·31	0·282565	39	0·00123	2	-7·0	0·282563	-5·4	1·4	–	-5·6
AW038-17·1	116	0·0020465	2	9·59	0·31	0·282604	34	0·00108	1	-6·7	0·282602	-3·9	1·2	–	-4·3
AW038-18·1	114	0·0020451	2	8·88	0·31	0·282583	25	0·00071	0	-6·4	0·282582	-4·6	0·9	–	-5·0
AW038-19·1	113	0·0020457	2	9·20	0·32	0·282622	77	0·00096	1	-6·1	0·282620	-3·3	2·7	–	-3·6
AW038-20·1	117	0·0020459	1	9·29	0·30	0·282632	35	0·00127	4	-5·7	0·282630	-2·9	1·2	–	-3·3
Y1-IG070 – Granite															
IG070-1·1	107	0·0020447	1	8·69	0·30	0·282582	32	0·00177	2	-10·0	0·282579	-4·9	1·1	–	-5·1
IG070-2·1	107	0·0020466	1	9·63	0·30	0·282528	37	0·00287	12	-11·9	0·282523	-6·9	1·3	–	-7·1
IG070-3·1	107	0·0020455	1	9·06	0·30	0·282574	39	0·00164	2	-10·2	0·282571	-5·2	1·4	–	-5·4
IG070-4·1	107	0·0020458	2	9·23	0·31	0·282583	34	0·00148	1	-10·6	0·282581	-4·9	1·2	–	-5·0
IG070-5·1	107	0·0020467	1	9·67	0·30	0·282586	43	0·00152	1	-9·1	0·282583	-4·8	1·5	–	-4·9
IG070-6·1	107	0·0020457	1	9·19	0·30	0·282561	33	0·00136	2	-9·5	0·282559	-5·6	1·2	–	-5·8
IG070-7·1	107	0·0020451	1	8·90	0·30	0·282608	36	0·00192	9	-9·1	0·282605	-4·0	1·3	–	-4·2
IG070-8·1	107	0·0020467	2	9·67	0·31	0·282575	37	0·00123	4	-8·8	0·282573	-5·1	1·3	–	-5·3
IG070-9·1	107	0·0020473	1	9·97	0·30	0·282576	41	0·00223	10	-8·5	0·282572	-5·2	1·5	–	-5·3
IG070-11·1	110	0·0020471	0	9·86	0·30	0·282555	35	0·00125	4	-8·2	0·282553	-5·8	1·2	–	-6·0
IG070-12·1	112	0·0020453	1	8·96	0·30	0·282613	44	0·00170	2	-7·9	0·282610	-3·7	1·6	–	-4·0
IG070-13·1	113	0·0020479	1	10·27	0·30	0·282551	36	0·00144	1	-7·6	0·282548	-5·9	1·3	–	-6·2
IG070-15·1	115	0·0020471	2	9·84	0·31	0·282587	40	0·00112	2	-7·3	0·282585	-4·5	1·4	–	-4·9

Notes:
^{176}Lu decay constant of $1·865 \times 10^{-11}$ (Soderlund *et al.* 2004).
$^{176}Hf/^{177}Hf$ and $^{176}Lu/^{177}Hf_{CHUR}$ values of 0·282785 and 0·0336, respectively (Bouvier *et al.* 2008).

Table 5: Compositions used for phase equilibria modelling

	Weight % (from XRF whole rock analyses)												
Sample	SiO_2	TiO_2	Al_2O_3	Fe_2O_3	FeO	MnO	MgO	CaO	Na_2O	K_2O	P_2O_5	LOI	Total
10CY-15	68.82	0.81	14.67	1.24	4.55	0.05	2.76	0.82	1.64	3.05	0.06	1.77	100.24
Y1-IG053	65.51	0.89	16.60	1.03	3.86	0.07	2.02	3.95	3.40	2.20	0.30	1.01	100.84
10CY-002	63.92	0.70	16.52	0.74	5.82	0.11	3.76	1.25	2.44	4.24	0.17	1.86	101.53
R7218	71.13	0.38	13.97	2.44	–	0.05	0.91	2.36	3.45	3.64	0.14	1.05	99.52

		Normalized molar proportions (mol.%)										
Sample	Figure	H_2O	SiO_2	Al_2O_3	CaO	MgO	FeO	K_2O	Na_2O	TiO_2	O	Total
10CY-15	6c	0.92	74.27	9.34	0.95	4.44	5.11	2.10	1.72	0.65	0.51	100
Y1-IG053	6d	1.59	69.84	10.43	4.51	3.21	4.26	1.50	3.52	0.71	0.42	100
10CY-002	6a	5.56	65.69	10.00	1.38	5.76	5.58	2.78	2.43	0.54	0.28	100
R7218	6b	3.70	75.24	8.71	2.67	1.44	1.94	2.46	3.54	0.30	0.10[a]	100

[a] *10% of iron assumed to be ferric. All other Fe^{2+}/Fe^{3+} values were determined by titration.*